

4

**NUMERICAL STUDIES OF
TURBULENT FREE SURFACE FLOWS AND
UNSTEADY PROPELLER FLOWS**

- Final Report on Contract N00014-90-C-0039 -

by

Steven A. Orszag
Vadim Borue
Ilya Staroselsky
Yansi Zhang



March 1995

Cambridge Hydrodynamics, Inc.
P. O. Box 1403
Princeton, NJ 08542
(609) 683-1515

DTIC QUALITY INSPECTED 5

19950526 045

DISTRIBUTION STATEMENT A

Approved for public release;
Distribution Unlimited

REPORT DOCUMENTATION PAGE		READ INSTRUCTIONS BEFORE COMPLETING FORM
1. REPORT NUMBER	2. GOVT ACCESSION NO.	3. RECIPIENT'S CATALOG NUMBER
4. TITLE (and Subtitle) Numerical Studies of Turbulent Free Surface Flows and Unsteady Propeller Flows		5. TYPE OF REPORT & PERIOD COVERED FINAL 01JAN90 — 31MAR95
		6. PERFORMING ORG. REPORT NUMBER
7. AUTHOR(s) Steven A. Orszag, Vadim Borue, Ilya Staroselsky, and Yansi Zhang		8. CONTRACT OR GRANT NUMBER(s) N00014-90-C-0039
9. PERFORMING ORGANIZATION NAME AND ADDRESS Cambridge Hydrodynamics, Inc. P. O. Box 1403 Princeton, NJ 08542		10. PROGRAM ELEMENT, PROJECT, TASK AREA & WORK UNIT NUMBERS
11. CONTROLLING OFFICE NAME AND ADDRESS Office of Naval Research 800 N. Quincy Street Arlington, VA 22217-5000		12. REPORT DATE 31MAR95
		13. NUMBER OF PAGES 60
14. MONITORING AGENCY NAME & ADDRESS (if different from Controlling Office)		15. SECURITY CLASS. (of this report) Unclassified
		15a. DECLASSIFICATION/DOWNGRADING SCHEDULE
16. DISTRIBUTION STATEMENT (of this Report) Approved for public release; distribution is unlimited		
17. DISTRIBUTION STATEMENT (of the abstract entered in Block 20, if different from Report)		
18. SUPPLEMENTARY NOTES		
19. KEY WORDS (Continue on reverse side if necessary and identify by block number) Turbulence Free-surface Renormalization group Eddy viscosity Large-eddy simulation Reynolds-averaging Navier-Stokes equations Unsteady flows Hydrofoil		
20. ABSTRACT (Continue on reverse side if necessary and identify by block number) Two main problems have been studied, viz. the structure of turbulence near a free surface and the Reynolds-averaged solution of unsteady propellor/hydrofoil flows by the renormalization group (RNG) two-equation turbulence transport model. A variety of free-surface turbulence simulations demonstrate the key modifications in turbulence structure due to the free surface. In addition, we determine the modifications in surface wave spectra due to the turbulence beneath the free surface as typically represented by a renormalized dispersion relation. The results for unsteady hydrofoils show the power of the RNG method in robustly and accurately treating large-scale unsteady and transitional flows, a marked improvement over previous turbulence transport models.		

DD FORM 1 JAN 73 1473

SECURITY CLASSIFICATION OF THIS PAGE (When Data Entered)

Chapter 1

Introduction

Accession For	
NTIS	CRA&I <input checked="" type="checkbox"/>
DTIC	TAB <input type="checkbox"/>
Unannounced <input type="checkbox"/>	
Justification	
By	
Distribution /	
Availability Codes	
Dist	Avail and/or Special
A-1	

In this Report, we summarize results obtained with support of ONR Contract N00014-C-90-0039. Two general classes of problems are studied. First, we have performed a variety of numerical simulations of turbulence in the presence of a free surface. Second, we have performed Very Large Eddy Simulations of the turbulent flow past prototype propeller configurations.

The structure of turbulence interacting with a free surface is an important problem for a variety of Navy applications. First, the free surface may have significant effects on the structure of turbulence and thereby effect transport properties in ocean environment. Such knowledge is important to understand such varied characteristics as sound propagation, transport of nutrients, contaminants, and other tracers in the upper ocean. Second, the turbulence may itself affect free surface characteristics. Such effects may influence our ability to discern sub-surface phenomena from observations of the surface waves. Such information is critical for the proper interpretation of sea-surface observations obtained via various remote sensing techniques. Third, the basic structure of free surface turbulence has remained a hitherto relatively unexplored area in which advances may influence our fundamental understanding of turbulence processes.

In Section 2 we summarize our results on free surface turbulence through a variety of simulations of turbulent channel flows with a free surface.

In Section 3, we survey our numerical methods for solving moving boundary problems using spectral elements and finite volume techniques. In particular, we describe the RNG $K-\epsilon$ model for treatment of transport processes in turbulence.

In Section 4, we report results of Very Large Eddy Simulations of turbulent flow past prototype propeller configurations. In particular, we concentrate attention on the so-called MIT flapping foil experiment in which an oscillating NACA16 hydrofoil is studied. This example has the advantage that it has been widely studied previously using alternative turbulence models and has an extensive and well documented database associated with it. The flapping foil experiment has been a difficult one for previous modeling efforts using traditional two-equation turbulence models, in the sense that it has been necessary to fix a number of *ad hoc* modeling parameters to achieve agreement with even some of the experimental data. In this report we show that the RNG-based two-equation transport model does an excellent job of predicting such key turbulent flow characteristics as skin friction coefficient C_f without adjustable parameters. These results offer the prospect that the RNG turbulence model will become a standard for use in Naval Architecture community. To this end, we have worked to ensure that the VLES RNG model is available in a well supported, user-friendly, generally available code environment. This will help to facilitate the broad application of our work to a variety of propeller design problems.

Chapter 2

Interaction of Surface Waves with Free Surface Turbulent Flow

Here we describe numerical simulations of incompressible unsteady open-channel flow. The main goal of this study was to investigate the effects of mutual interaction of surface waves with in-depth turbulence, especially the influence of near-surface turbulence upon dispersion, propagation, and statistics of the waves.

2.1 Problem Background

Free-surface turbulent flows are of genuine interest for ocean technology. This problem bridges surface wave phenomena and fully developed hydrodynamic turbulence. For the most part, previous studies of surface wave phenomena have concentrated on the behavior of non-dissipative, although highly dispersive and nonlinear, ensembles of waves. In this case, potential flow is a good approximation since molecular viscosity is important only within a thin boundary layer $l_v \approx 2\pi(\nu^2/g)^{1/3}$ which is normally much smaller than all the characteristic scales such as the capillary length or system dimensions. It is usually assumed that, inside this viscous layer, large vorticity is generated. These vortex sheets move with

the surface but play a rather minor role in the large-scale surface dynamics. Their role, however, may be important in small-scale ocean-air interaction, e.g. short gravity waves, capillary waves and wind generated ripples. At the same time, dissipation and vorticity generation phenomena are essential within the turbulent fluid.

Here, we concentrate upon the effects of the mutual influence of random surface waves and statistical properties of the near free surface (FS) region in fully developed turbulent flow. To date, there is no comprehensive strong coupling theory of these phenomena. Numerical simulations reported here were done using spectral methods and capitalize upon the success of early numerical experiments experiments for wall-bounded flows.

At the present time, there exist rather extensive experimental studies of turbulent open channels (Ueda *et al.* 1977; Nezu & Rodi 1986; Kirkgoz 1989), as well as semi-empirical theories and results of $K - \mathcal{E}$ and Reynolds stress modeling (Gibson & Rodi 1989; Celik & Rodi 1984; Swean *et al.* 1991). The advantage of the DNS approach taken here is its independence of any *ad hoc* assumptions often necessary for theory to progress and its greater flexibility in matching experimental conditions. Our studies focused upon channel flow bounded with a rigid wall from below and having an open upper surface. Some DNS calculations of open channel flow were already performed in Handler *et al.* (1991), Leighton *et al.* (1991) and Swean *et al.* (1991). However, in those early works only the case of zero Froude number was considered. The numerical scheme used in our simulations coincides in the case of zero Froude number with that of Swean *et al.* (1991). In our work we mostly concentrate on the study of the nonzero Froude number case.

In the following sections, we will formulate our approach to the problem, then describe the numerical scheme, and present the results of flow simulations.

2.2 Strategy of Full Navier-Stokes Simulation of the Turbulent Free-Surface Problem

We solve the three-dimensional Navier-Stokes equation for incompressible flow:

$$\partial_i v_i = [\mathbf{v} \times \boldsymbol{\omega}]_i - \nabla_i \pi + \nu \Delta v_i \quad (2.1)$$

$$\frac{\partial v_i}{\partial x_i} = 0$$

where \mathbf{v} is the velocity field, p is the pressure, $\pi = p/\rho + v^2/2$, ν is the kinematic viscosity and ρ is the density of fluid. The boundary conditions are:

$$v_i|_{\text{rigid wall}} = 0 \quad (2.2)$$

$$n_i \tau_{ij}|_{\text{free surface}} = n_i \tau_{ij}|_{\text{ext}}$$

where $\tau_{ij} = -p\delta_{ij} + \nu\rho(\partial_i v_j + \partial_j v_i)$ are the internal and external components of the stress tensor respective to the fluid, and n_i is the normal to the free surface (and summation over repeated indices is implied). The system (2.1), (2.2) is closed using the equation for the free surface height h :

$$\partial_t h + v_\alpha \cdot \partial_\alpha h = v_{\text{normal}}|_{fs} \quad (2.3)$$

Here an index denoted by a Greek letter α corresponds to directions in the free surface (the $x - y$ plane) and ∂_α stands for the differentiation in that direction. If we consider a channel, the rigid wall is located at $z = -H/2$, the upper boundary of the physical domain is given by $z = H/2 + h(x, y, t)$, and the subscript fs designates values taken at the free surface.

Our goal is to use high-resolution spectral methods. When this technology is applied to a flow bounded between two rigid walls, the flow is reproduced by a Fourier spectral series in the $x - y$ direction and by a Chebyshev polynomial representation in the z -direction. The latter concentrates collocation points towards the walls, providing high resolution

of boundary layers. However, in an open channel the upper surface is curved and time-dependent, which complicates the use of spectral methods. One possible approach is to give up the high resolution in the z -direction provided by using the Chebyshev polynomials. However, we believe that it is essential to ensure proper resolution of near-free-surface boundary layers.

The approach used here is based upon linearization of the boundary conditions at the free surface. Then the boundary conditions (2.2) are adjusted to those imposed at the unperturbed surface. Such an approach retains the ability to use of the Chebyshev spectral method in the z -direction to achieve high resolution. The boundary conditions then take the form

$$\begin{aligned}\partial_t h + \partial_\alpha (h v_\alpha) &= v_z \\ \rho \nu (\partial_\alpha v_z + \partial_z v_\alpha) &= \tau_{\alpha z}|_{ext} \\ gh - \sigma_* \Delta h + 2\nu \partial_z v_z &= \frac{p}{\rho} - \frac{p_{ext}}{\rho}\end{aligned}\tag{2.4}$$

where g is the gravitational constant, $\sigma_* = (\sigma/\rho)$ is the surface tension, $\tau_\alpha|_{ext}$ and p_{ext} are the external stress and pressure, respectively. All terms in (2.4) are evaluated at $h(x, y, t) = 0$; again the index α means that only horizontal components are used. The only nonlinear term retained in (2.4) is the term $\partial_\alpha (h v_\alpha)$ responsible for the convection of the free surface by the horizontal velocity. It turns out that in our formulation the convective term is the same order of magnitude as v_z though $\partial_\alpha h$ is small. Equations (2.1) and (2.4) represent the final formulation of the boundary problem that we use here to describe open surface turbulent flow. In linear approximation, this system reproduces both the dispersion relation of surface waves and the Helmholtz instability at the surface. Interaction effects are accounted for by the nonlinearity of the Navier-Stokes equation. The ability to describe effects of nonlinear self-interactions of surface waves, a separate problem which is outside the scope of this project, is sacrificed when we use the present approach.

2.2.1 Applicability limits

First of all, a linear analysis (Landau & Lifshitz 1987) shows that, for each spatial harmonic with a wave-number k and the amplitude h , linear approximation of the boundary conditions is only valid when $h \leq l_w$, where $l_w = (2\nu/\Omega(k))^{1/2}$ and $\Omega(k) = (gk + \sigma_* k^3)^{1/2}$. It may be seen later that Fourier spectrum of $h(k)$ is rather steep and the condition $kh(k) \leq l_w$ is automatically satisfied whenever it is valid at the smallest wave-numbers. This leads to the estimate for the flow 'integral' Froude number (here and later $\sigma_* = 0$ is assumed)

$$F_i = U/(gH)^{1/2} << 10/Re^{1/3}, \quad (2.5)$$

Here this integral Froude number and the Reynolds number $Re = UH/\nu$ are defined using the centerline velocity U and the channel height. Deriving (2.5) we assumed that $h \approx u_{rms}^2/2g$. We also assumed that in the range of flow Reynolds numbers of interest here, $Re \approx 10^3 - 10^4$, the characteristic rms velocity at the surface can be heuristically estimated as $u_{rms} \approx 10^{-1}U$ (Kim, Moin & Moser 1987).

At the same time it would not be satisfactory to consider only waves that are shorter than the viscous sublayer width l_v and whose amplitude are smaller than l_v . The dissipation length of waves l_v is defined as the scale where the frequency of wave is equal to the wave decay rate (see (2.17) below). If that was the case, our analysis would only be of general methodological interest and not applicable to the description of real phenomena in water waves. Indeed, in water at normal conditions, $l_v \approx 10^{-2}cm$, whereas the capillary length $d = (2\sigma_*/g)^{1/2} = 10^{-1}cm$. It is clear that any length scales smaller than d are not of interest for engineering and oceanographic applications because they are effectively damped by capillary effects.

The condition for the existence of wave motion is $l_v \leq h$, resulting in the inequality

$$F_i \geq 10/Re^{1/2}, \quad (2.6)$$

It is clear that, as $Re \rightarrow \infty$ there exists a wide range of Froude numbers where both inequalities (2.5) and (2.6) hold. It is worth mentioning that in a typical flow of engineering

interest ($H \approx 1m$, $U \approx 0.1m/s$, $Re \approx 10^4$, $Fi \approx 10^{-1}$) the condition (2.5) is satisfied. This is also the case for a typical laboratory setup in free-surface-flow studies of Ueda *et al.* 1977.

2.3 Spectral Methods for Free Surface Turbulence

A spectral method, with Fourier series in the streamwise (x) and spanwise (y) directions, and Chebyshev polynomial expansion in the normal direction (z), is employed spatially. A conventional time-splitting scheme is used to separate nonlinear and viscous time steps. However, the solution for incompressibility and viscosity is done within the same step by solving a fourth-order equation for the normal velocity and a second-order equation for the normal component of vorticity. Streamwise and spanwise velocity components are recovered from the incompressibility condition. If we define the Reynolds number as $Re = UH/\nu$, the convective term as $\hat{v}_i = [\mathbf{v} \times \boldsymbol{\omega}]_i$ and the normal component of vorticity as $\psi = \partial v_x / \partial y - \partial v_y / \partial x$, (2.1) takes the form:

$$\frac{\partial}{\partial t} \nabla^2 v_z = f_v + \frac{1}{Re} \nabla^4 v_z, \quad (2.7)$$

$$\frac{\partial}{\partial t} \psi = f_\psi + \frac{1}{Re} \nabla^2 \psi, \quad (2.8)$$

where

$$f_v = \Delta \hat{v}_z - \frac{\partial}{\partial z} \text{div}(\hat{\mathbf{v}})$$

and

$$f_\psi = \text{rot}_z(\hat{\mathbf{v}}).$$

Here the incompressibility condition has already been taken into account.

The boundary conditions at the wall are:

$$\psi|_{\text{wall}} = v_z|_{\text{wall}} = \frac{\partial}{\partial z} v_z|_{\text{wall}} = 0 \quad (2.9)$$

The boundary conditions at the free surface are more complicated. The conditions on the tangential components of stresses (see (2.4)) can be expressed straightforwardly in the

form:

$$\frac{\partial}{\partial z} \psi|_{fs} = Re \left(\frac{\partial}{\partial x} \tau_{yz}|_{ext} - \frac{\partial}{\partial y} \tau_{xz}|_{ext} \right) = W_{rot} \quad (2.10)$$

$$\frac{\partial^2 v_z}{\partial z^2}|_{fs} - \nabla_\alpha^2 v_z|_{fs} = -Re \left(\frac{\partial}{\partial x} \tau_{xz}|_{ext} + \frac{\partial}{\partial y} \tau_{yz}|_{ext} \right) = W_{div} \quad (2.11)$$

where the subscript α again indicates horizontal components. The third boundary condition on v_z is obtained through the relation on pressure at the surface. In our numerical scheme, the pressure computation is not required for time advancement. Should data on pressure be needed for turbulent statistics, it can be calculated by two different, but essentially equivalent ways. One can either use the equation for the normal component of velocity v_z with the wall pressure values determined from an equation for $\partial_\alpha v_\alpha$, or one can use the equation for $\partial_\alpha v_\alpha$ with the pressure corresponding to zero wave-numbers determined from the v_z -equation. Therefore, it is convenient to impose the pressure boundary condition in the following form:

$$\frac{\partial}{\partial t} \partial_z v_z = \Delta_\alpha \pi - \partial_\alpha \hat{v}_\alpha + \frac{1}{Re} \Delta (\partial_z v_z) \quad (2.12)$$

$$\pi = gh - \sigma_* \Delta h + \frac{2}{Re} \partial_z v_z + \frac{v^2}{2} - p_{ext}$$

Here the equation for $\partial v_z / \partial z$ is obtained from the equation for $\partial_\alpha v_\alpha$.

Time stepping is carried with a semi-implicit scheme involving a Crank-Nicolson scheme for the viscous terms and Adams-Bashforth scheme for the nonlinear terms. For the time advancement of surface height we use a Crank-Nicolson scheme for the normal velocity component and an Adams-Bashforth scheme for the convective term (Canuto *et al.* 1987). Equation (2.8) then reduces to

$$\left(1 - \frac{\delta t}{2Re} \nabla^2 \right) \psi^{n+1} = \frac{\delta t}{2} (3f_\psi^n - f_\psi^{n-1}) + \left(1 + \frac{\delta t}{2Re} \nabla^2 \right) \psi^n \quad (2.13)$$

with the boundary conditions (2.9), (2.10). Equation (2.13) is solved by the Chebyshev-tau method for each horizontal Fourier component of the vorticity field.

The fourth-order equation (2.7) is solved by splitting it into two second-order equations

$$\left(1 - \frac{\delta t}{2Re} \nabla^2\right) \phi^{n+1} = \frac{\delta t}{2} (3f_v^n - f_v^{n-1}) + \left(1 + \frac{\delta t}{2Re} \nabla^2\right) \phi^n \quad (2.14)$$

$$\nabla^2 v_z^{n+1} = \phi^{n+1}$$

with the boundary conditions (2.9), (2.11) and the pressure boundary condition (2.12) which has the following form:

$$\partial_z v_z^{n+1} - \partial_z v_z^n = \frac{\delta t}{Re} \partial_z^3 v_z^{n+1/2} + \frac{3\delta t}{Re} \nabla_\alpha^2 v_z^{n+1/2} + \delta t \nabla_\alpha^2 (g_* h^{n+1/2} - p_{ext}) + \frac{3}{2} \eta^n - \frac{1}{2} \eta^{n-1}. \quad (2.15)$$

Here we use the following notations:

$$v_z^{n+1/2} = 1/2(v_z^{n+1} + v_z^n),$$

$$h^{n+1/2} = 1/2(h^{n+1} + h^n),$$

$$g_* = g + \sigma_*(k_x^2 + k_y^2) \quad \text{and}$$

$$\eta = \delta t \left(\partial_\alpha \hat{v}_\alpha - \nabla_\alpha^2 \frac{v^2}{2} \right).$$

The time advancement scheme for surface height is

$$\begin{aligned} h^{n+1} - h^n &= \frac{\delta t}{2} (v_z^{n+1} + v_z^n) - \frac{\delta t}{2} (3f_h^n - f_h^{n-1}) \\ f_h &= \frac{\partial}{\partial x_\alpha} (v_\alpha h(x_\alpha)) \end{aligned} \quad (2.16)$$

The system of coupled equations (2.14), (2.16) and (2.9), (2.11), (2.15) is solved by the Chebyshev-tau method, in which the four boundary conditions are satisfied by means of a Green's function technique. This system requires three Green functions G_i . The first two of them solve the equations

$$\begin{aligned} \left(1 - \frac{\delta t}{2Re} \nabla^2\right) \hat{G}_{1,2} &= 0 \\ \nabla^2 G_{1,2} &= \hat{G}_{1,2} \end{aligned}$$

with the boundary conditions

$$\Delta G_1|_{fs} = G_1|_{fs} = G_1|_{wall} = 0;$$

$$\Delta G_1|_{wall} = 1;$$

and

$$\Delta G_2|_{wall} = G_2|_{wall} = 0;$$

$$G_2|_{fs} = 1;$$

$$\frac{\partial^2 G_2}{\partial z^2}|_{fs} = -k^2 G_2|_{fs}.$$

In order to take into account the 'tau correction', i.e. numerical errors due to the finite number of retained Chebyshev polynomials, it is necessary to introduce a third Green function G_3 which satisfies the equation

$$\Delta G_3 = 0$$

with the boundary condition

$$G_3|_{wall} = 0;$$

$$G_3|_{fs} = 1.$$

The third Green function G_3 is used to satisfy equations at the boundary points and the boundary conditions at the same time.

To avoid aliasing errors involved in computing the nonlinear terms pseudo-spectrally, the usual 2/3 dealiasing procedure is used.

The computations reported here were performed on

The accuracy of the numerical code was examined in two different ways. First we implemented the numerical scheme for closed channel flow and analyzed the time evolution of small-amplitude Orr-Sommerfeld modes. In all the tests performed both linear decay and growth rates were predicted with errors of less than $10^{-2}\%$. In the second set of tests, we analyzed the decay in time of an infinitesimally small wave with given wave number k

at the free surface. We measured the frequency $\Omega(k)$ and the decay rate $\Gamma(k)$ of the wave and compared them with the theoretical prediction for small amplitude deep water waves (Landau & Lifshitz 1987)

$$\Omega(k) = (gk + \sigma_* k^3)^{1/2}; \quad \Gamma(k) = 2\nu k^2. \quad (2.17)$$

Equation (2.17) is valid when $\Gamma \ll \Omega$, which is always the case for our range of parameters. It was shown that the frequency $\Omega(k)$ is reproduced by the numerical scheme very accurately (usually in the range of $10^{-1} - 10^{-2}\%$), provided the time step δt is small enough $\Omega(k)\delta t \leq 0.2$. Our numerical time advancement scheme has second order accuracy in time. Since $\Gamma \ll \Omega$ it is necessary to decrease δt even further if we want to obtain the correct value for the decay rate of waves. It may be shown that significant numerical dissipation may be avoided if $\delta t \Omega(k) \leq (\Gamma(k)/\Omega(k))^{1/2} \approx (l_v k)^{3/4}$. Under this restriction, which is generally not so burdensome, we obtained a decay rate that differs from the theoretical one by only $10^{-1}\%$. In all our runs, we chose the time step small enough to correctly reproduce the dynamics of the surface waves.

2.4 Computational Data

We consider a setup where turbulence is generated through an externally imposed pressure gradient in the x direction which supplies the centerline mean velocity U . The initial velocity fields were obtained from the standard Orr-Sommerfeld instability modes for channel flow. The flux in the x direction, i.e. the bulk mean velocity

$$U_m = \frac{1}{2} \int_{-1}^1 \langle v_x \rangle dz = \frac{2}{3},$$

was fixed by adjusting the mean pressure gradient. The viscosity is chosen to be $\nu = 1/3000$ and the maximum mean velocity $U_{max} \approx 0.765$. The Reynolds number defined through the maximum mean velocity is $Re \approx 4560$. The wall-shear velocity is

$$u_* = \left(\frac{\tau_{wall}}{\rho} \right)^{1/2} = \left(\nu \frac{\partial u_x}{\partial z} \Big|_{wall} \right)^{1/2} \approx 0.041$$

so that $Re_* = (u_* H)/\nu \approx 250$.

Under these conditions, the Kolmogorov dissipation wave-number estimated via the energy dissipation rate at the centerline, $\mathcal{E} \approx 5 \times 10^{-5}$ is $k_d = (\mathcal{E}/\nu^3)^{1/4} \approx 35$ and is smaller than the maximum wave-number in the $x - y$ plane. This means that turbulence in the bulk of the channel and near the rigid wall is well resolved. We believe that the near-free-surface region is also resolved properly. Indeed, the Froude number F_i in our runs varied from 0.1 to 0.6, and the corresponding boundary layer was thick enough to contain several Chebyshev collocation points. (although l_v is less than the Kolmogorov dissipation scale). Both criteria (2.5) and (2.6) hold in this case and the linearization of the boundary conditions is well based.

2.4.1 Turbulence statistics

The mean velocity profile is shown in Figure 1. In Figure 1, the velocity is normalized by the wall-shear velocity u_* and the distance from the rigid wall z_+ is measured in wall units $z_+ = zu_*/\nu$. As expected the mean velocity profile obeys the law of the wall $u_+ = 2.5 \ln z_+ + 5.5$ starting from approximately $z_+ = 30$. Typically, the mean velocity is slightly larger than one would expect from the law of the wall just near the free surface, in accordance with the data Nezu & Rodi (1986). Such deviations are likely to result from the effects of the free surface. The data plotted in Figure 1 corresponds to a typical run with Froude number $F_i \approx 0.55$.

Turbulence intensities and Reynolds shear stress normalized by the wall-shear velocity are shown in Figures 2 and 3, respectively. The data on rms vorticity is shown in Figure 4. Near the rigid wall and close to the centerline, the profiles are in good agreement with the DNS data on rigid-wall channel flow (Kim, Moin & Moser 1987) and in reasonable agreement with experimental data (Kreplin & Eckelmann 1979). For example, the intensity of streamwise turbulent fluctuations peaks at $z_+ \approx 13$. We have compared our measurements for the skin friction coefficient $C_f = \tau_{wall}/\frac{1}{2}U_m^2$ with the experimental correlations proposed by Dean (1978). The friction coefficient in our case is found to be

$C_f \approx 7.6 \times 10^{-3}$. This agrees well with Dean's formula $C_f \approx 0.073 Re_m^{-0.25} \approx 7.7 \times 10^{-3}$ where $Re_m = 2HU_m/\nu \approx 8000$. The ratio U_{max}/U_m is 1.148, also in a good agreement with Dean's data $U_{max}/U_m = 1.28 Re_m^{-0.0116} = 1.153$. The comparison with available data on turbulence intensities in open channel flow (Nezu & Rodi 1986) also shows good agreement. The streamwise rms velocity at the free surface in wall units is roughly 1 in our study and 0.8 – 1.2 in the experiments and the spanwise rms velocity is roughly 0.7 and 0.65, respectively.

An important outcome of our study is that within the feasible range of Froude numbers (2.5), typical mean flow profiles do not change significantly with the flow Froude number. Turbulence intensities and rms vorticity data are also weakly sensitive to the Froude number. We may conclude that for small Froude numbers it is reasonable to consider even the limiting case $F_i = 0$. Such flow in which the gravitation constant g is infinite can be visualized as corresponding to a half-channel flow with two rigid walls, where the inviscid, no-stress boundary conditions are imposed at the wall corresponding to the 'free surface' (Hunt & Graham 1978). The presence of such a no-stress wall is the dominant effect at small Froude numbers. In this sense, the free surface responds nearly linearly to the bulk turbulence and does not lead to significant changes in the fluid flow near the free surface compared with the case $F_i = 0$. The dependencies on the flow Froude number are only significant in the near-free-surface region of the size $l_w = (2\nu/\Omega_h)^{1/2}$, where Ω_h is some characteristic frequency of turbulence at the free surface. These effects are discussed further in the next Section.

The most important influence of the free surface is that the fluid motion near the free surface is quasi two-dimensional. The fluctuations of the velocity normal to the surface are substantially smaller than the ones in horizontal directions. The only component of vorticity that is large near the free surface is that normal to the free surface. We may expect that the most important excitations of the free surface come from vortex tubes attached to the free surface at one end, produced by small scale eddies of nearly two-dimensional turbulence. In this case, an inverse energy cascade may take place that may facilitate the

formation of large vortex tubes near the free surface.

Turbulent eddy viscosity in the near free surface region

Using data on the Reynolds stress and mean velocities, we obtained distributions of eddy viscosity in open surface flow. A typical profile of eddy viscosity is plotted in Figure 5 at $F_i = 0.55$.

First, we compared our data with the empirical formula

$$\frac{\nu_{eddy}}{\nu H_+} = 0.4 \frac{z}{H} \left(1 - \frac{z}{H}\right). \quad (2.18)$$

A comparison of (2.18) with experimental data for open channel flow was made by Ueda *et al.* (1977). Eq. (2.18) implies that the law of the wall is valid throughout the channel, which is certainly not true at least near the rigid wall. From Fig.5, we see that the measured distribution is rather well described by (2.18) near the free surface.

We have analyzed the dependence of eddy viscosity upon the turbulent kinetic energy K and the energy dissipation rate \mathcal{E} . Our recent developments in renormalization group turbulence modeling suggest that the mean rate-of-strain dependence of eddy viscosity is also important (Yakhot *et al.* 1992). We found the following expression to be in good agreement with the present data:

$$\nu_{eddy} = C_\mu \frac{K^2}{\mathcal{E}} \frac{2}{1 + (\eta/a)^2}, \quad (2.19)$$

where

$$\eta = \frac{du_x}{dz} \frac{K}{\mathcal{E}}.$$

Using turbulent characteristics K and \mathcal{E} measured from the simulations, we find that the best choice of numerical constants is $C_\mu = 0.09$, $a = 3.0$. The dimensionless parameter η is the ratio of turbulent to mean strain time scale. Near the rigid wall η is large (≈ 25); in the log-layer of the channel η is approximately constant (between 3 and 4); near the free surface η approaches zero. As the results plotted in Fig. 5 suggest, the interpolation formula (2.19) holds rather well near the rigid wall. Close to the free surface, the eddy

viscosity given by (2.19) differs significantly from the measured data, due to the decrease of energy dissipation rate caused by the zero stress boundary conditions.

2.4.2 Details of near-free-surface behavior

Our results show that the viscous term in the boundary condition (2.12) is numerically small and $p_{rms} \approx gh_{rms}$, where $h_{rms} = \langle h^2 \rangle^{1/2}$ is the rms surface height. On the other hand, the rms pressure at the free surface $p_{rms} \approx \langle v_i^2 \rangle / 2$ is approximately independent of g (see Fig. 6). Therefore, the following approximate relation is well satisfied:

$$h_{rms} \approx \frac{K_{fs}}{g}, \quad (2.20)$$

where K_{fs} is the mean kinetic energy at the surface.

Another observation is that the root mean-square fluctuations of the streamwise and spanwise velocity components, as well as the normal component of vorticity are practically independent of g , whereas $v_z|_{rms} \sim 1/g$. The rms values of streamwise and spanwise components of vorticity are also inversely proportional to g . The scaling of u_z with g and (2.20) suggest that there exists a characteristic frequency of surface height fluctuations $\Omega_h|_{rms} \approx v_z|_{rms} / h_{rms}$ which is approximately constant in the range of Froude numbers considered. This frequency relates to the characteristic turnover times of the largest turbulent eddies. Within the viscous sublayer, the turbulent kinetic energy K was observed to be practically independent of the distance from the free surface. Therefore, the Neumann boundary condition $\partial K / \partial z = 0$ seems to be relevant for modeling free-surface phenomena.

Most of the averaged quantities or their derivatives vary smoothly in the middle of the channel but vary nearly exponentially near the free surface. To analyze their behavior, it is convenient to define an operator $\hat{\mathcal{F}}$ of the following form:

$$\hat{\mathcal{F}}(f(z_{fs})) = \frac{f(z_{fs}) - f(\infty)}{f(0) - f(\infty)}. \quad (2.21)$$

The operator $\hat{\mathcal{F}}$ acts on functions $f(z_{fs})$, where z_{fs} designates the distance from free surface. According to the definition, $\hat{\mathcal{F}}(f(0)) = 1$ for any f . For functions which fall off

exponentially away from the free surface, $\hat{\mathcal{F}}(f(z_{fs})) \approx \exp(-z_{fs}/\lambda)$. In Figure 7, we show the near-free-surface behavior of different flow characteristics analyzed by means of the limiting operator $\hat{\mathcal{F}}$. Plotted in Figure 7 are the mean rate of strain $\langle dv_x/dz \rangle$, the energy dissipation rate \mathcal{E} , the horizontal components of rms vorticity $\omega_{x,y}^{rms}$, as well as the z -derivatives of the Reynolds stress $\langle d(v_x v_z)/dz \rangle$. Most of these characteristics change exponentially near the free surface as $\sim C_1 - C_2 \exp(-z_{fs}/\lambda)$ with approximately the same exponent $\lambda \approx 0.08H$. If we identify λ with a depth of some skin-layer, a characteristic excitation frequency at the free surface can be estimated as $\Omega_0 \approx 2\nu/\lambda^2$. In our setup, such estimation gives $\Omega_0 \approx 0.42$. It is shown later that this frequency nearly matches the directly measured characteristic frequency of surface wave motion.

As may also be seen from Figure 7, the ratio of the turbulent kinetic energy $K(z_{fs})/K(0)$ and the ratio of rms normal vorticity fluctuations $\omega_z^{rms}(z_{fs})/\omega_z^{rms}(0)$ are approximately constant.

2.4.3 Surface waves on top of turbulent flow

Dispersion relations.

Let us define two correlation functions of some variable $q(x, t)$

$$U_q(k) = \int \langle q(x, t)q(0, t) \rangle \exp(ikx) dx \quad (2.22)$$

$$S_q(k, \Omega) = \int \langle q(x, t)q(0, 0) \rangle \exp(ikx + i\Omega t) dx dt \quad (2.23)$$

so that $U_q = \int (d\Omega/2\pi) S_q$. Here k stands for the wave-vector in the horizontal plane and all quantities are evaluated at the free surface. The correlation functions U_q are directly measured in our numerical experiments, whereas the evaluation of the functions S_q requires rather expensive time averaging. In our case, a linearized version of (2.3) yields:

$$S_h(k, \Omega) = \frac{1}{|\Omega|^2} S_{v_z}(k, \Omega), \quad (2.24)$$

and for the equal-time spectral densities:

$$U_h(k) = \int \frac{1}{|\Omega|^2} S_{u_z}(k, \Omega) \frac{d\Omega}{2\pi}. \quad (2.25)$$

In the low- k region ($k \ll 1/l_w$), the singularities of correlation function S_h are dominated by the oscillatory part of dispersion relation. Using Equation (2.17), we obtain

$$U_h(k) = C(k)U_{v_z}(k), \quad C(k) = \frac{1}{|\Omega|^2(k)}. \quad (2.26)$$

At this point, it is important to mention that the spectra U_h and U_z themselves may be far from those corresponding to the linear surface waves problem. Also the relation (2.26) does not require potentiality of the surface flow. The only assumption that was used in the derivation of (2.26) is that the Green function for the equation for normal velocity has a pole at the characteristic frequency given by (2.17), whereas the dissipative term in the dispersion relation is negligible. Such an assumption may become invalid due to the effects of turbulence. Also, the effects of the mean flow in our case can, in principle, complicate the dispersion relation structure. The ratio

$$\Omega_h(k) = \left(\frac{U_{v_z}(k)}{U_h(k)} \right)^{1/2} \quad (2.27)$$

may be called a characteristic frequency of surface height excitations at wave number k . Measurements of the spectra (2.27) can serve as a diagnostic tool to analyze the properties of near-free-surface turbulence.

In Figure 8, we show the two-dimensional spectrum of the logarithm of characteristic wave frequencies. The shape of the spectrum is practically isotropic in the $k_x k_y$ - plane so that the dispersion relation can be well represented by the 'one-dimensional' spectrum shown in Figure 9. The one-dimensional spectrum is obtained from the isotropic two-dimensional spectrum by summing all the $U_q(k)$ with k on a circle of a given radius $|k|$. When $k/k_d \geq 1$, the measured dependence $\Omega_h(k)$ is well described by (2.17). At smaller wave numbers, the function $\Omega_h(k)$ deviates significantly from (2.17) and reaches an approximately constant value Ω_0 . This behavior of the characteristic frequency reflects the influence of 'bottom-generated' turbulence upon the surface wave behavior. The wave spectra in the low k region $k/k_d \leq 1$ are forced by the turbulence. The frequency Ω_0 depends on the flow Reynolds number only and characterizes the frequency of the attached vortex tubes. In the turbulence dissipation range, nonlinear effects are small and surface waves

can be considered as freely evolving. It should be noted that the numerical value of the limiting frequency $\Omega_0 = \Omega(k \rightarrow 0) \approx 0.5$ is close to the estimate obtained in Section 4.2.

Spectral exponents.

The spectra of surface height $h(k)$, and velocity components $v_{x,y}(k), v_z(k)$ are also isotropic in wave-number space. The one dimensional spectra are plotted in Figure 10. Spectral behavior of the surface height correlation function differs significantly from the Phillips' surface wave spectral laws $1/k^3$ (Phillips 1977) or $1/k^{7/2}$ (Phillips 1985). In fact, the spectral index is between one and two. This fact is not very surprising, because we are mostly concerned with spectra of small surface waves forced by the bulk turbulence. Linearization of the free surface boundary definitely contribute to this discrepancy. Surface waves in our problem play the role of a diagnostic tool that enable us to measure spectral characteristic of bulk turbulence. On the other hand, Phillips' spectrum may be observed in the so-called wave saturation range for waves in the ocean, where nonlinear wave interaction is essential. Our data are in reasonable agreement with the low Froude number data of Brumley & Jirka (1987) where the spectra of free-surface velocity fluctuations were measured for the case of grid generated turbulence with a grid at the bottom of the tank.

For all Froude numbers that we considered, the characteristic surface frequencies Ω_h were lower than the free-surface frequencies (2.17). When the gravitational constant g decreases, these frequencies match and resonant excitations of the surface waves occur.

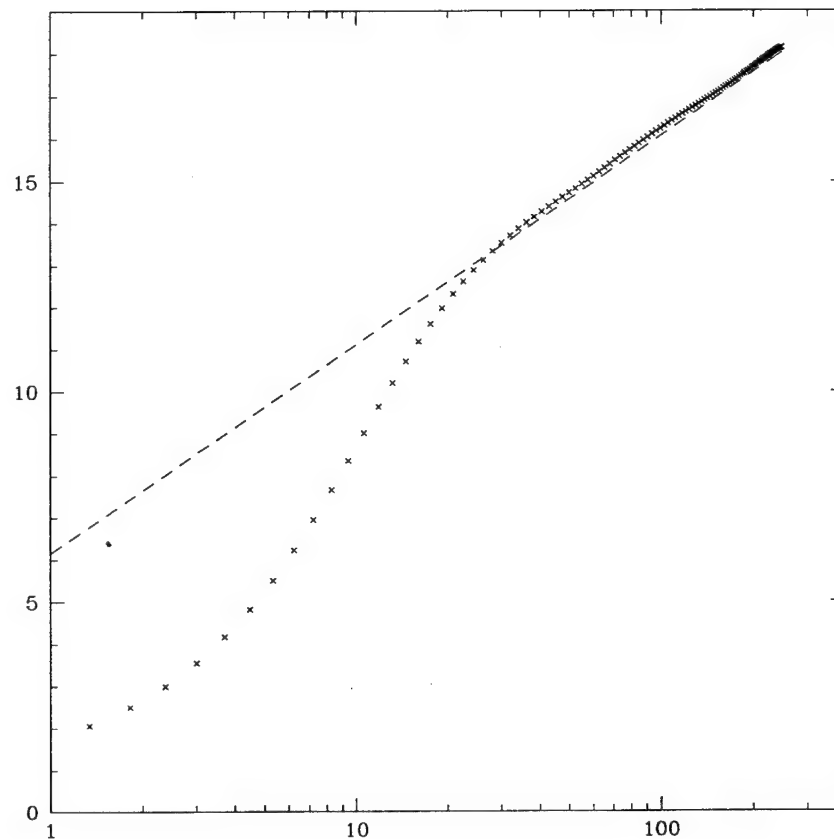


Figure 2.1: Mean-velocity profile, $z_+ = 0$ corresponds to the rigid wall; the dashed line is the law of the wall $u_+ = 5.5 + 2.5 \ln z_+$; $U_{max}/u_* = 18.6$, $U_{max}/U_m = 1.148$

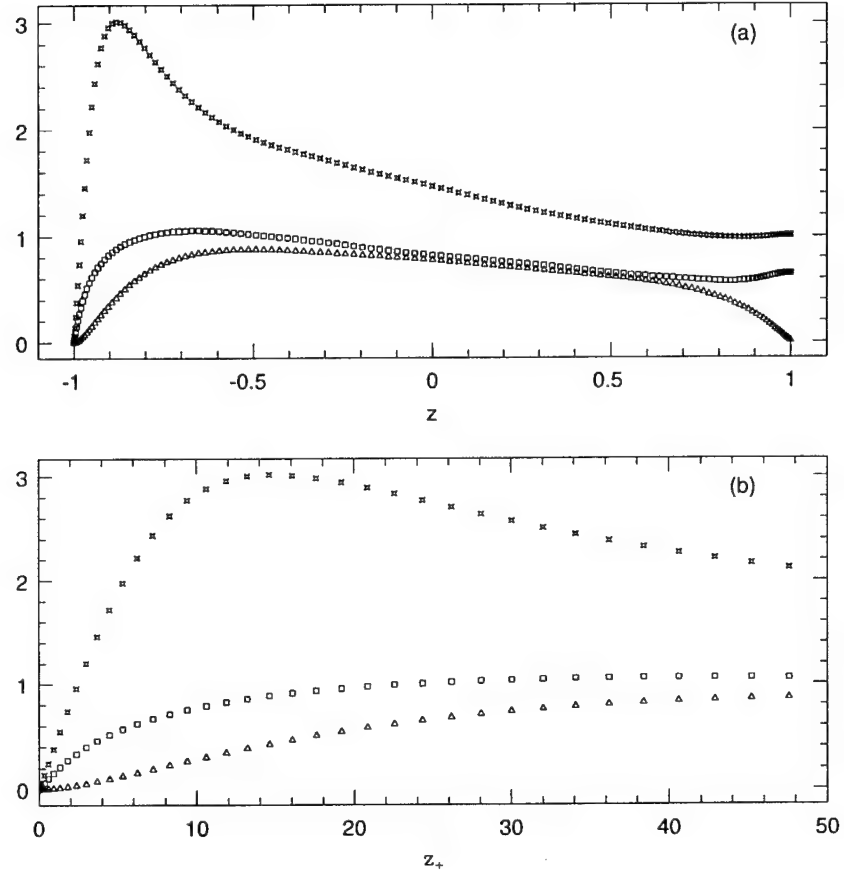


Figure 2.2: Root-mean-square velocity fluctuations normalized by the wall shear velocity: \times , v_x^{rms} ; \square , v_y^{rms} ; \triangle , v_z^{rms} . (a) in global coordinates; (b) in wall coordinates.

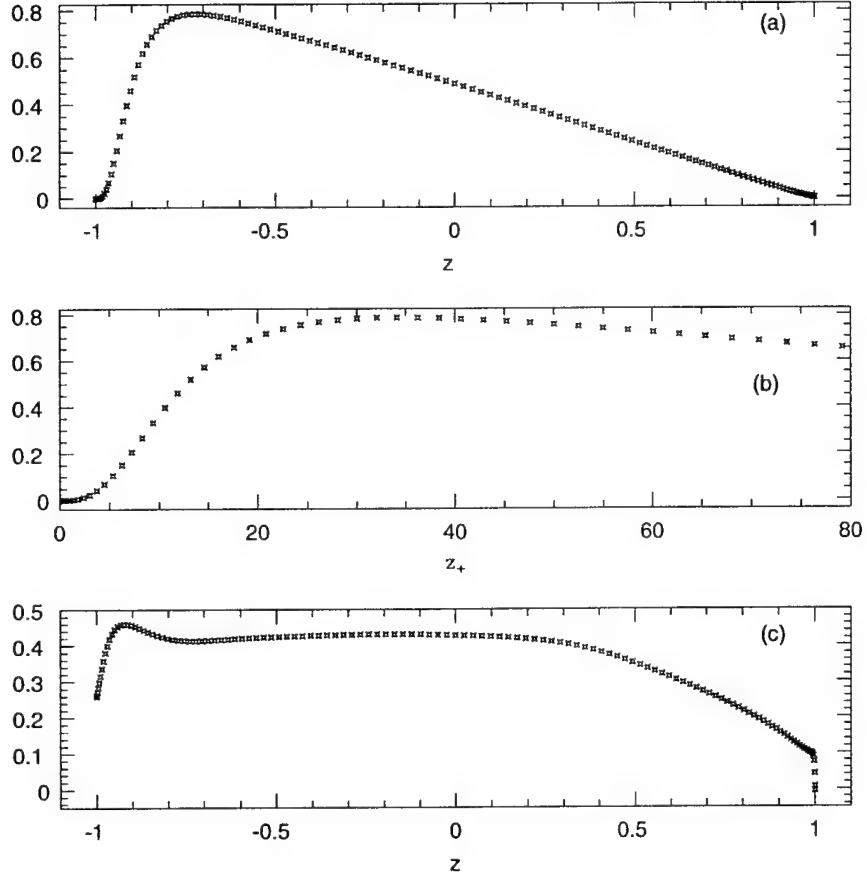


Figure 2.3: Reynolds stress $-\langle v_x v_z \rangle$: (a) in global coordinates; (b) in wall coordinates. Correlation coefficient $-\langle v_x v_z \rangle / v_x^{rms} v_z^{rms}$: (c) in global coordinates.

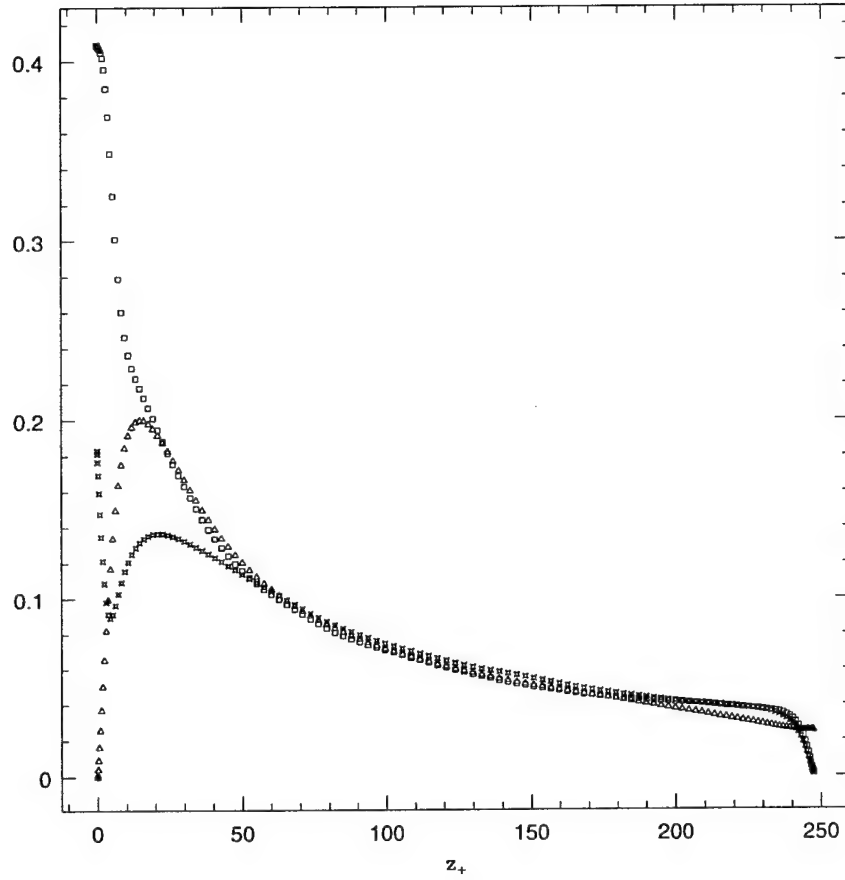


Figure 2.4: Root-mean-square vorticity fluctuations normalized by the mean shear: \times , $\omega_x \nu / u_*^2$; \square , $\omega_y \nu / u_*^2$; \triangle , $\omega_z \nu / u_*^2$ in wall coordinates.

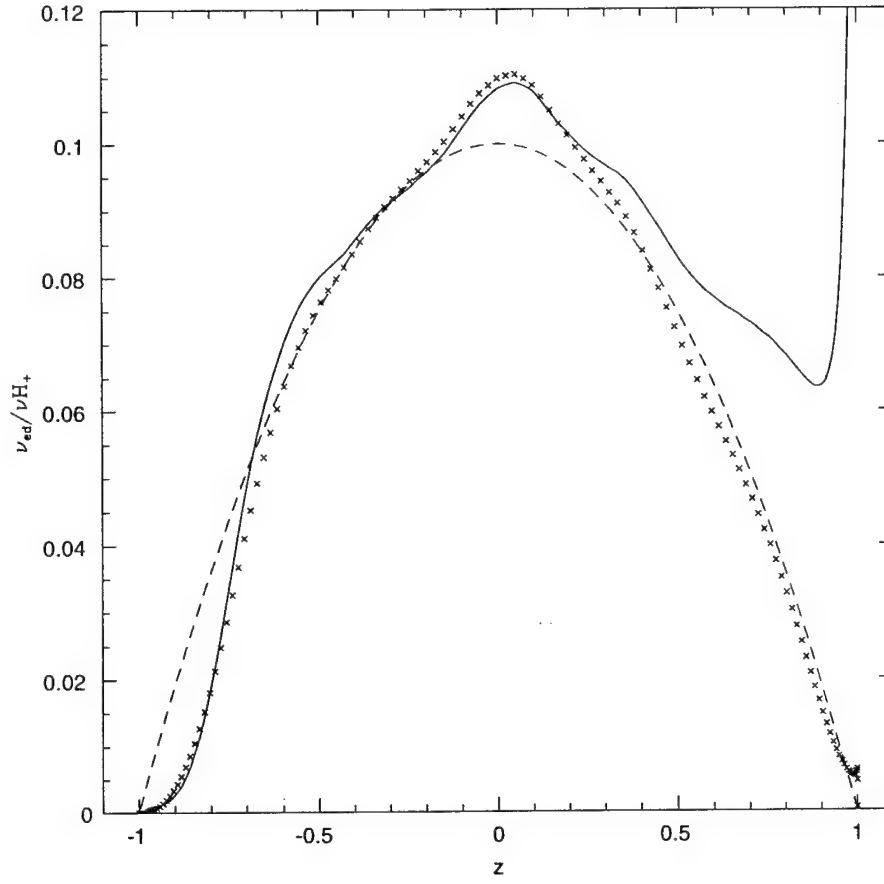


Figure 2.5: Distribution of eddy viscosity $\frac{\nu_{eddy}}{\nu H_+}$ in open channel flow. Crosses - measurements. Dashed line - (18) Solid line - (19) model.

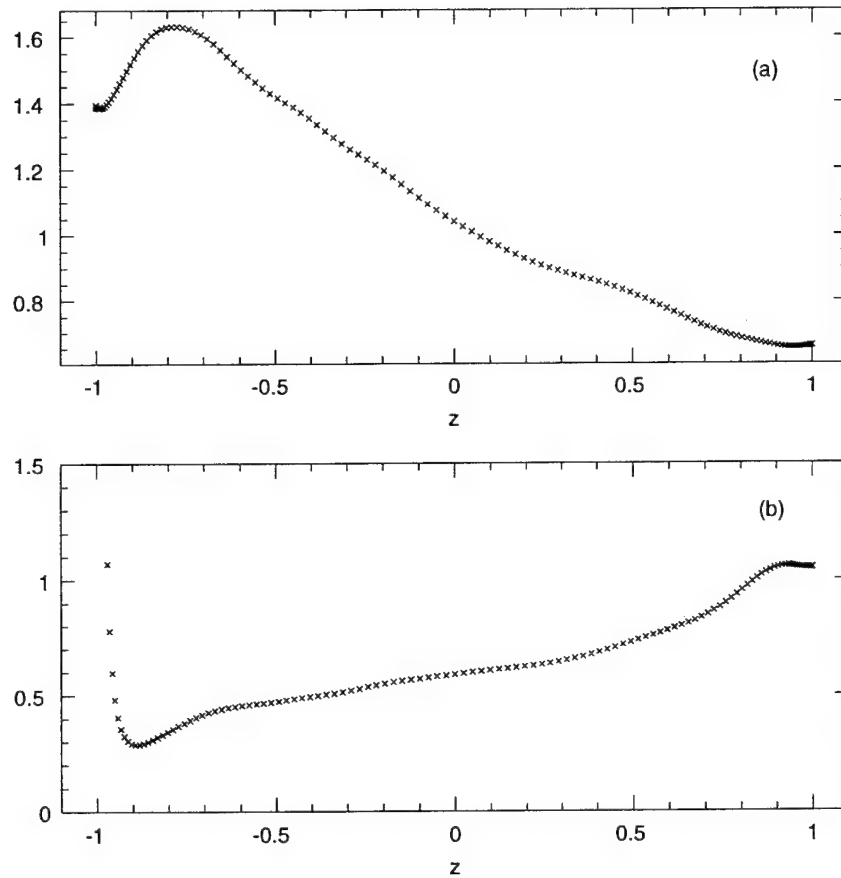


Figure 2.6: (a) Root mean-square pressure fluctuations normalized by the wall shear velocity p_{rms}/u_*^2 ; (b) Ratio of root mean-square pressure fluctuations to the mean kinetic energy.

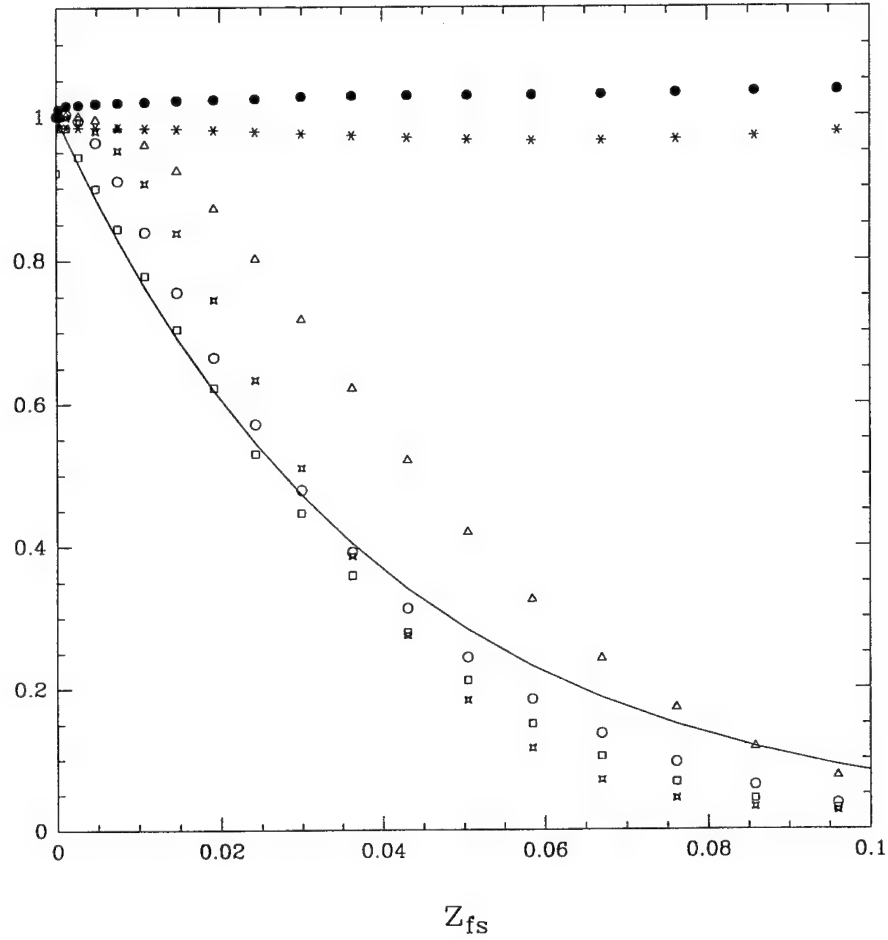


Figure 2.7: Near-free-surface behavior of flow characteristics. The limiting operator $\hat{\mathcal{F}}$ is applied to: \times , \mathcal{E} ; Δ , $\langle d(v_x v_z)/dz \rangle$; \square , $\langle dv_x/dz \rangle$; o , $\omega_{x,y}^{rms}$. The ratios of $K(z_{fs})/K(0)$ and $\omega_z^{rms}(z_{fs})/\omega_z^{rms}(0)$ are shown by $*$ and \bullet , respectively. Solid line is $e^{-z_{fs}/\lambda}$ with $\lambda \approx 0.08H$. z_{fs} is the distance from the free surface.

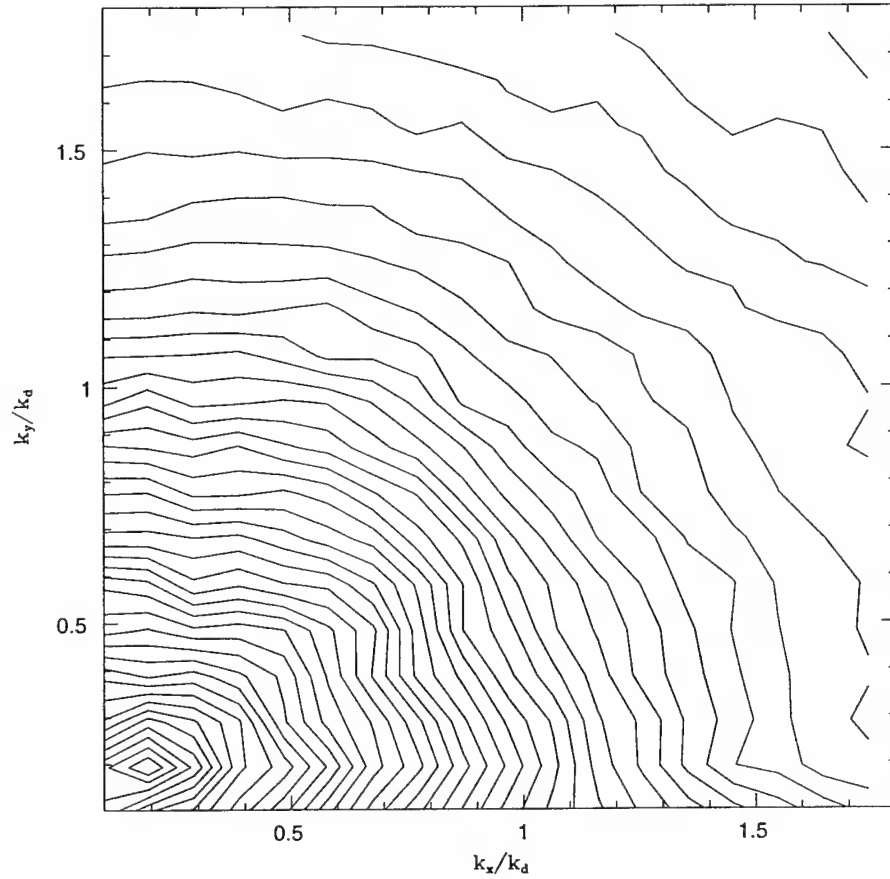


Figure 2.8: Two-dimensional spectrum of characteristic surface frequencies. Lines of constant $\log(\Omega_h(k))$ as the function of k_x/k_d , k_y/k_d are shown.

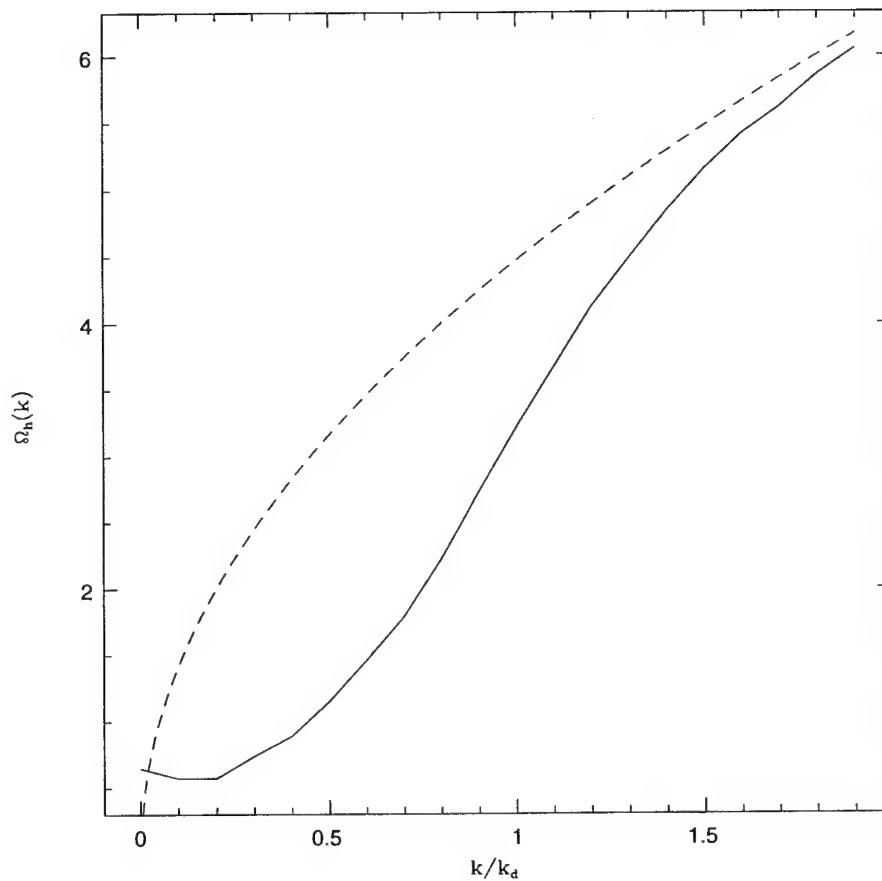


Figure 2.9: Spectra of characteristic surface frequencies $\Omega_h(k)$ as the function of k/k_d for $F_i \approx 0.55$ (solid line). The dashed line is $\Omega(k) = (gk)^{1/2}$.

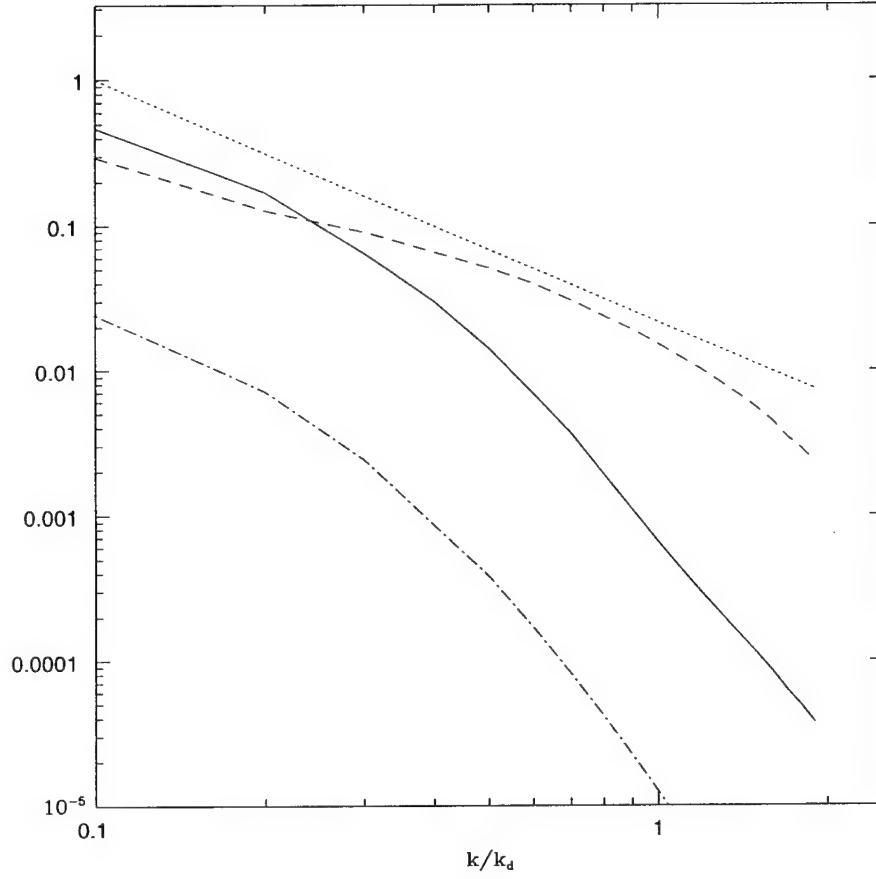


Figure 2.10: One dimensional spectra of surface height correlator $U_h(k)/h_{rms}^2$ (solid line); the normal velocity at the surface correlator $U_{v_z}(k)/\langle v_z^2 \rangle|_{fs}$ (dashed line); the tangential velocity at the surface correlator $10^{-1}U_{v_{x,y}}(k)/\langle v_{x,y}^2 \rangle|_{fs}$ (dot-dashed line) as the function of k/k_d . Dot line is $1/k^{5/3}$.

Chapter 3

Computational Methods

3.1 Variational formulation of spectral elements method for flows with moving boundaries

Here we outline the technical details involved in implementation of the free moving boundary problem. We consider simulation of incompressible flows involving free surfaces which can be moving in time. The equations of motion are the incompressible Navier-Stokes equations:

$$\frac{\partial \mathbf{v}}{\partial t} + (\nabla \cdot \mathbf{v})\mathbf{v} = \nabla \cdot \boldsymbol{\sigma} = -\nabla p + \nu \nabla^2 \mathbf{v} \quad (3.1)$$

$$\nabla \cdot \mathbf{v} = 0 \quad (3.2)$$

In order to develop spatial discretization, let us derive the variational form of the Navier-Stokes equations when the whole mesh (or part of the mesh) is moving with a velocity \mathbf{w} . Consider the motion of fluid in a time-dependent control volume $\Omega(t)$ moving with the velocity \mathbf{w} . The mesh velocity \mathbf{w} is chosen so that it minimizes the deformation of the domain Ω . According to Reynolds transport theorem:

$$\frac{d}{dt} \int_{\Omega(t)} (\psi * \mathbf{v}) d\omega = \int_{\Omega(t)} \frac{\partial}{\partial t} (\psi * \mathbf{v}) d\omega + \int_{\partial\Omega(t)} (\mathbf{n} \cdot \mathbf{w}) (\psi_s * \mathbf{v}) ds \quad (3.3)$$

Here, ψ is a vector test function and $*$ denotes collocation products where no summation is assumed. This way, one obtains from the first right hand side term that

$$\frac{\partial}{\partial t}(\psi * \mathbf{v}) = \psi * \frac{\partial \mathbf{v}}{\partial t} + \mathbf{v} * \frac{\partial \psi}{\partial t} \quad (3.4)$$

The first term on the right side of equation (3.4) can be substituted from equation (3.2), whereas the second term on the right side $\partial\psi/\partial t$ is only due to the motion of the domain with velocity \mathbf{w} and can therefore be replaced by

$$\frac{d\psi}{dt} = \frac{\partial\psi}{\partial t} + \mathbf{w} \cdot \nabla \psi = 0 \quad (3.5)$$

This way we obtain from (3.3), (3.5), and the divergence theorem that

$$\frac{d}{dt} \int_{\Omega(t)} (\psi * \mathbf{v}) d\omega = \int_{\Omega(t)} \psi * \frac{\partial \mathbf{v}}{\partial t} d\omega - \int_{\Omega(t)} \mathbf{v} * (\mathbf{w} \cdot \nabla \psi) d\omega + \int_{\Omega(t)} \nabla \cdot (\mathbf{w}(\psi * \mathbf{v})) d\omega \quad (3.6)$$

and by expanding the second term on the right and substituting from equation

$$\begin{aligned} \frac{d}{dt} \int_{\Omega(t)} (\psi * \mathbf{v}) d\omega &= \int_{\Omega(t)} \psi * \nabla \cdot (\boldsymbol{\sigma} - \mathbf{v}\mathbf{v}) d\omega - \int_{\Omega(t)} \mathbf{v} * (\mathbf{w} \cdot \nabla \psi) d\omega \\ &+ \int_{\Omega(t)} \psi * (\nabla \cdot \mathbf{w}\mathbf{v}) d\omega + \int_{\Omega(t)} \mathbf{v} * (\mathbf{w} \cdot \nabla \psi) d\omega \end{aligned} \quad (3.7)$$

and by integration by parts of the first right hand side term,

$$\frac{d}{dt} \int_{\Omega(t)} (\psi * \mathbf{v}) d\omega = \int_{\Omega(t)} \psi * \nabla \cdot (\mathbf{w}\mathbf{v} - \mathbf{v}\mathbf{v}) d\omega - \int_{\Omega(t)} \boldsymbol{\sigma} \cdot \nabla \psi d\omega + \int_{\partial\Omega(t)} (\mathbf{n} \cdot \boldsymbol{\sigma}) \psi_s ds \quad (3.8)$$

which is the variational form of the flow equations for a domain $\Omega(t)$. The spatial discretization then proceeds by defining the test functions ψ to be the Legendre Lagrangian interpolants used for Legendre spectral elements, and by obtaining the discretized set of equations.

3.1.1 RNG large-eddy simulations

Using this approach, we have simulated a number of massively separated flows in curved geometries. An efficient spectral element-Fourier code was developed and the RNG subgrid model was incorporated into it in order to provide a platform for large eddy simulations.

Flow past a spherical surface: Validation tests were performed in the low Reynolds number regime where the flow exhibits the large scale unsteadiness persisting in the high Reynolds number regime, and the results compare very favorably with experimental results ($Re \leq 1,000$). In the high Reynolds number regime, large eddy simulation was performed at $Re = 20,000$. This flow is characterized by a large scale vortex street and a complex small scale flow structure in the near wake. The time behavior of the drag coefficient was highly unsteady with the characteristic frequency of approximately twenty times the Strouhal frequency in agreement with the available experimental data.

3.2 Implementation of Transport models

We have implemented the renormalization group theory $K - \epsilon$ transport model on a finite volume platform which handles arbitrarily complex geometries using curvilinear coordinate systems. The main advantage of using a finite volume discretization is that, being a low order method, it is very efficient, in terms of both speed and memory. In addition, since the main purpose of turbulence transport modeling is to solve for an average field where all small scale fluctuations in space and time are smoothed out, the optimal dispersive and diffusive properties of spectral elements (or other spectral-type global methods) are not really needed. On the other hand, because of the global character of the spectral-type methods which couple many points together, it is extremely difficult to implement special treatment close to walls when using low Reynolds number models which are essential for the non-equilibrium regions. Finite volume methods allow for local use of wall layers and direct control of grid size, necessary for the low Re number wall models.

Even in the case of large eddy simulation (LES), where no separate equations are solved

for the turbulent kinetic energy and energy dissipation rate, there is certain ambiguity in the definition of the resolvable flow length scale (the cut-off of filter function) in spectral-type methods. This is a direct consequence of the global character of spectral methods and the absence of a well defined local grid size, in contrast with the finite volume methods, where the grid size is obvious.

3.2.1 Formulation of the model

The incompressible Reynolds-Averaged Navier-Stokes (RANS), closed by the RNG $\mathcal{K} - \mathcal{E}$ model is given by

$$\frac{\partial \bar{U}_i}{\partial t} + \bar{U}_j \nabla_j \bar{U}_i = -\nabla_i P + \frac{\partial}{\partial x_j} [\nu_T (\frac{\partial \bar{U}_i}{\partial x_j} + \frac{\partial \bar{U}_j}{\partial x_i})]$$

$$\nabla_i \bar{U}_i = 0$$

$$\frac{\partial \mathcal{K}}{\partial t} + \bar{U}_j \nabla_j \mathcal{K} = \nu_{eddy} S^2 - \mathcal{E} + \nabla \alpha \nu_T \nabla \mathcal{K}$$

$$\frac{\partial \mathcal{E}}{\partial t} + \bar{U}_j \nabla_j \mathcal{E} = C_{\epsilon_1} \frac{\mathcal{E}}{\mathcal{K}} \nu_{eddy} S^2 - C_{\epsilon_2} \frac{\mathcal{E}^2}{\mathcal{K}} - R + \nabla \alpha \nu_T \nabla \mathcal{E}$$

where $\nu_T = \nu_{eddy} + \nu_{mol}$ and the rate of strain term R is given by

$$R \equiv 2\nu_{mol} S_{ij} \frac{\partial u_i}{\partial x_j} \frac{\partial u_j}{\partial x_i}$$

which is expressed in RNG $\mathcal{K} - \mathcal{E}$ model as

$$R = \frac{C_\mu \eta^3 (1 - \eta/\eta_0)}{1 + \beta \eta^3} \frac{\mathcal{E}^2}{\mathcal{K}}$$

where $\eta = S\mathcal{K}/\mathcal{E}$ and $S^2 = 2S_{ij}S_{ij}$ is the magnitude of the rate-of-strain.

These equations are incorporated in a code which solves the governing partial differential equations for the conservation of mass and momentum, as well as the transport of turbulent kinetic energy and the rate of dissipation. A general form of the above PDEs can be written

in Cartesian tensor notation as

$$\frac{\partial}{\partial t}(q) + \frac{\partial}{\partial x_i}(u_i q) = \frac{\partial}{\partial x_i} \left[\Gamma_q \frac{\partial q}{\partial x_i} \right] + S_q$$

where q is the conserved quantity. The equations are discretized by integration over the grid cells which results in a set of algebraic equations of the following general form:

$$q_P \sum_i (A_i - S_P) = \sum_i (A_i q_i) + S_C$$

where the summation is over the neighboring cells. The A - coefficients contain contributions from the convective and diffusive fluxes whereas S_C and S_P are the components of the linearized source term, $S_q = S_C + S_P q_P$. A second order power law difference scheme is used for the interpolation between grid points and calculation of the derivatives. The set of corresponding algebraic equations is solved by Patankar semi-implicit iterative schemes using relaxation. The sequence of iteration steps is as follows:

1. The momentum equations are solved using current values for pressure, in order to update the velocity field.
2. The Poisson equation is derived from the continuity equation and the linearized momentum equations. This "pressure correction" equation is then solved to obtain the necessary corrections to the pressure and velocity fields such that the continuity is achieved.
3. The \mathcal{K} and ϵ equations are solved using the updated velocity and the current value of eddy viscosity. Then the eddy viscosity is updated.
4. Check for convergence. Convergence is reached when the sum of normalized residuals falls below certain value. For a general variable q , the normalized residual is defined as:

$$\bar{R} = \frac{\sum_{nodes P} |A_E q_E + A_W q_W + A_N q_N + A_S q_S + S_C - A_P q_P|}{\sum_{nodes P} |A_P q_P|}$$

where A_E, A_W, A_N, A_S are the coefficients which combine convection and diffusion through the control volume surrounding given point P . S_C and S_P are the components of the linearized source term. The summation here extends over all of the computational points.

Chapter 4

RNG Transport Modeling of Hydrofoil Flows

In our simulations of complex hydrofoil flow using the RNG transport model we have observed excellent agreement with the experimentally measured data, including the skin friction and surface pressure coefficients, the location of separation region near the trailing edge of the testfoil, the wake velocity profiles and the boundary layer profiles on the foils. At the same time, the RNG transport model has demonstrated significant superiority over the standard standard $K-\epsilon$ model which does equally good job on the mean flow prediction but overestimates the friction coefficient by a factor of 2. Here we will describe the experimental setup which was fully matched in our simulations, outline the numerical techniques, and analyze the computational data.

4.1 Outline of the Benchmark Experimental Setup

Experiments have been performed in the MIT Variable Pressure Water Tunnel to study the flow over an isolated two dimensional hydrofoil subject to steady loading and to vertical gust loading at high reduced frequency. A modified NACA16 hydrofoil with chord length of 18 inches and maximum thickness of 8.84% is mounted in the test section on the centerline

of the tunnel. It has a geometrical angle of attack of 1.18° . Upstream there are two flappers operating at the reduced frequency $\kappa = 3.6$ and with the amplitude of 6 degrees. The Reynolds numbers based on testfoil chord length and freestream velocity are 1.36×10^6 and 3.78×10^6 . Free stream turbulence intensity was measured in the empty test section and found to be 1%. Transition was artificially triggered at $x/C = 0.105$ on both suction and pressure sides using 0.05 inch diameter epoxy disks of 0.008 inch high and separated by 0.05 inch.

Velocity and surface pressure were measured using two-component Laser Doppler Velocimeter (LDV) and miniature pressure transducers. For the unsteady measurements, the value at each time step was recorded as tan average over 250 periods. There are 180 sample points over one period. The velocity and pressure data were accumulated over a "bounding-box" around the test-foil, as well as on the surface and at certain wake locations. Friction coefficients C_f data was deduced from surface boundary layer measurements. The standard deviations of the velocity data on the "bounding box" are 0.029 in the streamwise direction and 0.016 in the vertical direction. The unsteady pressure measurements had a standard deviation of 0.02 based upon absolute pressure. There were uncertainties in the unsteady pressure measurements – it was found that the harmonic content of the surface pressure responds to the flapper or driving frequency, rather than to the hydrodynamic parameter of reduced frequency. It is very possible that the flappers excited a mode of tunnel vibration which contaminated the higher harmonics of pressure measurements.

We have performed numerical computations for both steady and unsteady flows with Reynolds number(3.78×10^6). The experimental setup described above was fully simulated in our numerical model by incorporation of the data provided by the MIT experimental group.

4.2 Computational Grid, Initial and Boundary Conditions

The origin of the coordinate system is at the leading edge of the test foil, with the x -coordinate positive in the downstream direction. The computational domain covers the tunnel with the inlet positioned upstream of the leading edge at $x/C = -0.261$, which coincides with the location where experimental measurement of the flow data is available, and the outlet being downstream at $x/C = 2.5$. Here, C is the hydrofoil cord length. A C-type grid built around the test foil uses the total of 301x166 grid points. In order to assure the proper boundary layer resolution without wasting computational resources in the far flow region, the grid spacing has been adjusted by hyperbolic tangent functions:

$$\Delta s(I) = \frac{q(I)}{A + (1 - A)q(I)}$$

where:

$$q(I) = \frac{1}{2} \left(1 + \frac{\tanh\{\delta(\frac{I}{I_{max}} - \frac{1}{2})\}}{\tanh(\frac{\delta}{2})} \right)$$

and

$$A = \frac{\sqrt{\Delta s_{I_{max}}}}{\sqrt{\Delta s_I}}$$

As a result, the grid spacing near the surface of the test foil is much denser, with approximately 35 grid points in the boundary layer. It should be mentioned that as a result of this adjustment the grid spacing at the tunnel wall is too coarse to resolve any boundary layer features. However, at these high Reynolds number ($\approx 10^6$), the tunnel wall boundary layer is so thin that there is no influence upon the flow around test foil which is of interest here.

The spatial discretization is second-order accuracy. For unsteady flow, the time-stepping scheme is fully implicit first-order Euler, and hence absolutely stable. Assuming that $q_{i,j}$ is a time dependent scalar quantity at the (i, j) grid point, the time-discretization is done as follows:

$$q_{i,j}^{t_{n+1}} - q_{i,j}^{t_n} = f(q_{i,j}^{t_{n+1}})$$

Standard non-slip boundary conditions are applied on the foil surface and tunnel walls. Downstream of the test foil, we adopted the outlet boundary conditions which imply zero normal fluxes of all flow variables. The upstream velocities are incorporated from the experiment data. This data, however, is available only in the section between $y/C = -0.306$ and $y/C = 0.360$ while the tunnel walls are at $y/C = -0.525$ and $y/C = 0.525$. In the steady case, the experimental data was interpreted via cubic spline to computational grid points. In the region between tunnel wall and the flapper wake where the experimental data is not available, the uniform velocity profiles were assigned. In the case of unsteady flow, the MIT FFX experiment provided 180 velocity profile samples inside the flapper wake at the upstream boundary. We performed a harmonic analysis of the experimental data:

$$U(x, y, t) = \sum_{i=0}^{20} \hat{U}_i(x, y) \sin(i\omega t + \theta_i(x, y))$$

$$\hat{U}_i(x, y) = \sqrt{a_i^2 + b_i^2}$$

$$\theta_i(x, y) = \tan^{-1}\left(\frac{a_i}{b_i}\right)$$

$$a_i = \frac{1}{N} \sum_{n=0}^N U(x, y, t_n) \cos\left(\frac{in2\pi}{N}\right)$$

$$b_i = \frac{1}{N} \sum_{n=0}^N U(x, y, t_n) \sin\left(\frac{in2\pi}{N}\right)$$

and extracted 20 harmonics as the upstream boundary conditions. In the region between the flapper wake and the tunnel walls, we have taken two different extrapolations: 1) simply setting the zeroth harmonics of the velocities to their freestream value and setting all the multiple harmonics to zero, and 2) setting the zeroth harmonics to some freestream value and linearly extrapolating the amplitude and the phase of the first harmonics from the edge of the flapper wake data:

$$U(x, y_{outer}, t) = U_{\infty} + \hat{U}_1(x, y_{edge}) \sin(\omega t + \theta_1(x, y_{edge})).$$

Another alternative is:

$$\begin{aligned} U(x, y_{outer}, t) &= U_{\infty} \pm \hat{U}_1(x, y_{edge}) \frac{\cosh(\frac{\omega}{c}(2h \mp y_{outer}))}{\cosh(\frac{h\theta}{c})} \cos(\omega t + \theta_1(x, y_{edge})) \\ V(x, y_{outer}, t) &= \hat{V}_1(x, y_{edge}) \frac{\sinh(\frac{\omega}{c}(2h \mp y_{outer}))}{\cosh(\frac{h\theta}{c})} \sin(\omega t + \theta_1(x, y_{edge})) \end{aligned}$$

with all the higher harmonics set to zero. Finally, as for the steady case, profiles of all velocity harmonics were projected onto the computation grid using cubic spline fit.

4.3 Computational Results

4.3.1 Steady Flow

Figures 4.1 to 4.3 show the computed static pressure and velocity fields respectively. It takes about 10,000 iterations to achieve convergence when started from a uniform initial field. We discuss here various quantitative features of the steady flow.

Test box data and computational inlet profiles.

The available experimental data includes average velocities at several stations on the sides of three rectangular nested boxes surrounding the test foil. In each direction, the average space separation between the probes is about 0.2% ~ 0.3%. This data at the upstream face of the box was used to set up the inlet velocity conditions, as shown in Figure 4.4. The experimental data corresponding to the top, bottom and the downstream

faces of the middle box were used to compare the computed mean velocity field in the far field region. The data in Figure 4.5 to Figure 4.7 respectively is indicative of adequate grid resolution and satisfactory boundary condition setting.

Wake velocity profiles.

The wake velocity profile and flow inclination plotted in Figure 4.8 demonstrate good overall agreement with the experimental data. The relative flow angle computed using RNG $K - \epsilon$ model clearly shows that the flow direction above the test foil is not aligned with the geometric foil surface. In particular, the flow has separated in a certain region just upstream of the trailing edge. This pattern is confirmed by contour plots of the streamwise velocity around the foil trailing edge shown in Figure 4.11. It should be mentioned that the standard $K - \epsilon$ model completely fails to predict separation near the trailing edge, which is not surprising since the standard $K - \epsilon$ model tends to overpredict eddy viscosity so that the turbulence level inside the boundary layer is too high for the flow to separate. We plot in Figure 4.12 the turbulence kinetic energy predicted by both the standard $K - \epsilon$ model and the RNG $K - \epsilon$ model. Obviously, the standard $K - \epsilon$ model generates much stronger turbulence energy on the foil surface and into the near trailing edge wake region.

Surface pressure.

Figure 4.9 shows the surface pressure coefficients. The observed variations of the computed C_p curves when the angle of attack is adjusted between 1.18 and 1.34 degrees is probably due to the uncertainty in the experimental conditions.

Skin friction coefficients.

Obviously, prediction of the skin friction coefficients involves adequate quantitative description of the entire boundary layer and transitional region thus representing the ultimate test of a transport model performance. The RNG $K - \epsilon$ model has demonstrated undisputable superiority over the existing transport models.

In Figure 4.10, we plotted the comparison of skin friction coefficients computed using the standard and the RNG $K - \epsilon$ model against experimental measurements. On the suction side for $x/C \geq 0.389$, where experiment data were available, computation with

the RNG $K - \epsilon$ model produced excellent agreement while the computation results using standard $K - \epsilon$ model severely overpredicted the skin friction. The results from the RNG $K - \epsilon$ model predicted the separation point (shown by the location where skin friction first turns) at $x/C = 0.968$, whereas the experiment data showed the separation point between $x/C = 0.972$ and $x/C = 0.990$. On the other hand, standard $K - \epsilon$ model did not indicate any separation at all because it overproduces turbulence energy, as we have discussed above. The RNG $K - \epsilon$ model computation also predicted transition regions at $x/C \simeq 0.09$ on the suction side and at $x/C \simeq 0.13$ on the pressure side. Since the MIT experiment employed transition-tripping devices on the testfoil, rigorous comparison with the experiment data is not possible.

4.3.2 Unsteady Flow

The period of flapper motion is $T = \frac{1}{f} = 0.06217(s)$. We conducted time-step sensitivity study and found that $\Delta t = \frac{T}{64}$ is an adequate choice for the time step. The unsteady calculation usually started from a converged steady field and it would take typically about $3 \sim 4$ periods to reach a periodic state. For the purpose of time series analysis, 32 samples per period were taken in most of our numerical simulations. The total evolution time for the time-dependent structure was usually 4 periods.

Zeroth Harmonics

We compare the zeroth harmonics of C_p of unsteady flow and the C_p of steady flow in Figure 4.13. Our computation agrees well with the experimental data, except for the pressure side of the foil where there is $5\% \sim 10\%$ discrepancy in the region $\frac{x}{C} \geq 0.6$. For the most part of the foil, the steady C_p is in good agreement with the mean C_p of the unsteady flow. Figure 4.14 shows the skin friction coefficients from steady flow computation and the zeroth harmonics of the skin friction coefficients obtained in unsteady flow calculation. We observe that the averaged C_f in the unsteady flow agrees fairly well with its counterparts in the steady flow almost everywhere except for the transition region where the mean C_f of unsteady flow shows $\sim 15\%$ increase over the C_f of steady flow; the transition point on the

suction side is shifted forward in the streamwise direction by about 5% while the transition point on the pressure side of the foil almost does not change. Although the flapper frequency ($f_f = 16$) is close to the natural frequency of the flow $f_n = \frac{U_\infty}{C} \simeq 14$, the unsteadiness effect is minimal due to the fact that the amplitude of the unsteady vertical gust on the inlet is small ($\frac{v}{U_{infty}} = 0.022$). Our main conclusion is that the steady calculation faithfully reproduces the average quantities in the unsteady flow. Although further experimental and numerical study may improve the accuracy of setting inlet conditions in unsteady flows, we believe that for practical applications, steady state analysis based on the RNG VLES model will provide accurate quantitative description.

Higher harmonics

We compare the computed first harmonics of the surface pressure coefficient with the experimental data in Figure 4.15. The numerical data reproduces well the qualitative behavior. The observed 10% ~ 20% difference between the computational and experimental data for the harmonics amplitude is largely due to the sensitivity of the pressure harmonics to the time dependent inlet conditions. Indeed, after using a different interpolation of the inlet data, as well as the potential model approximation for the region between the flapper wake and the tunnel wall where experimental data is not available, we have found that the pressure harmonics amplitudes differ by the same 10% ~ 20%. Figure 4.16 shows the amplitude and the phase of the skin friction coefficients on the test foil surface. The amplitude shows a peak near the leading edge between $\frac{x}{C} = 0.08$ and $\frac{x}{C} = 0.16$; similar behavior of the higher harmonics amplitude has been confirmed by the RNG $K - \epsilon$ model computation. Incidentally, the zeroth harmonics shows that the unsteady flow undergoes transition in the same region.(see Figure 4.14).

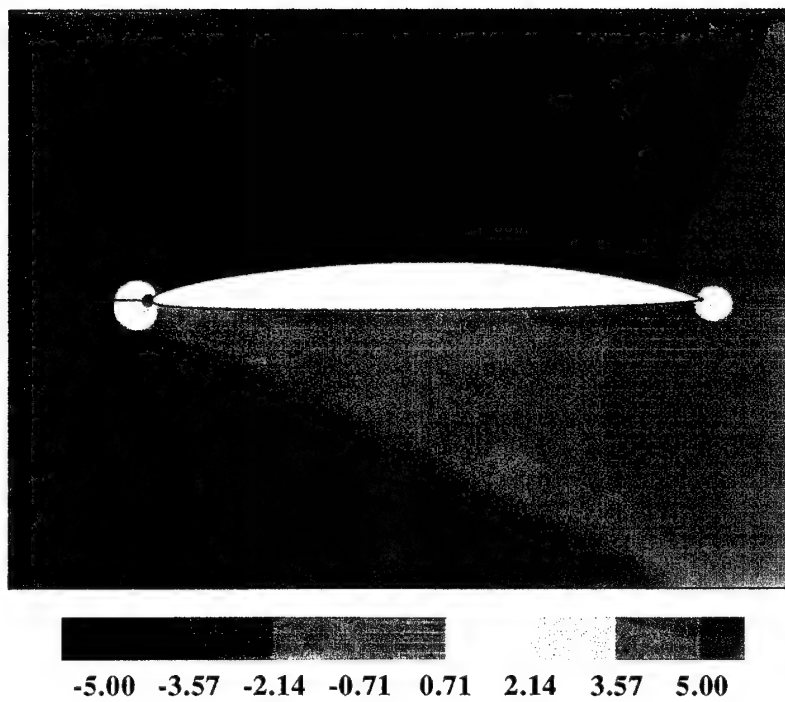


Figure 4.1: Steady flow static pressure contours around the foil.

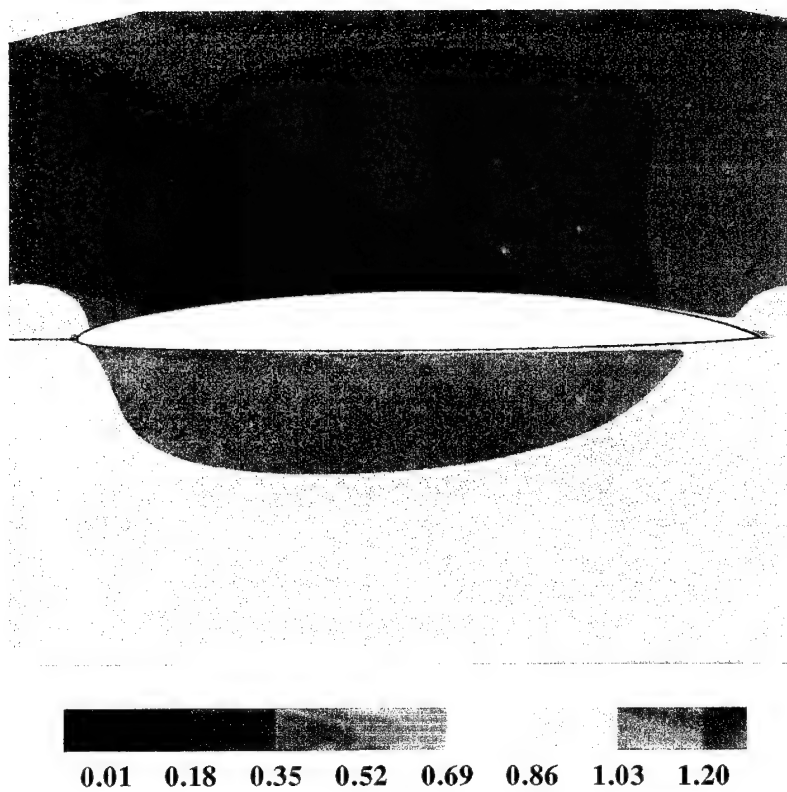


Figure 4.2: Steady flow streamwise velocity contours.

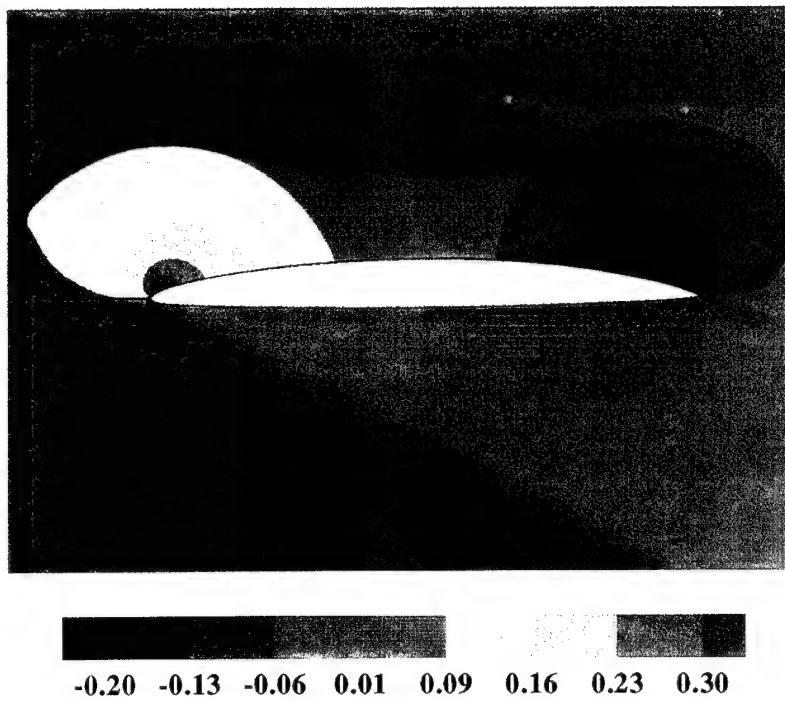


Figure 4.3: Steady flow vertical velocity contours.

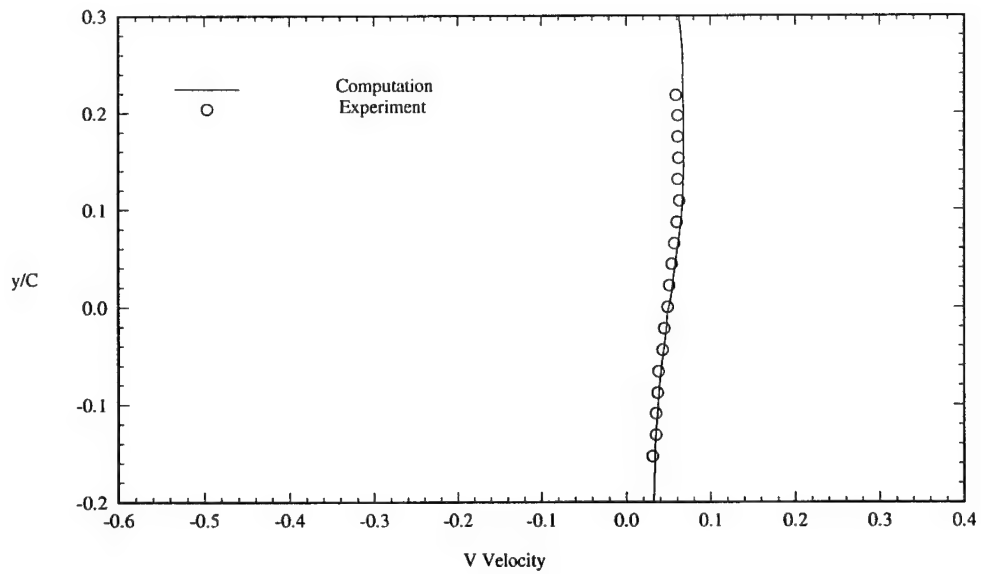
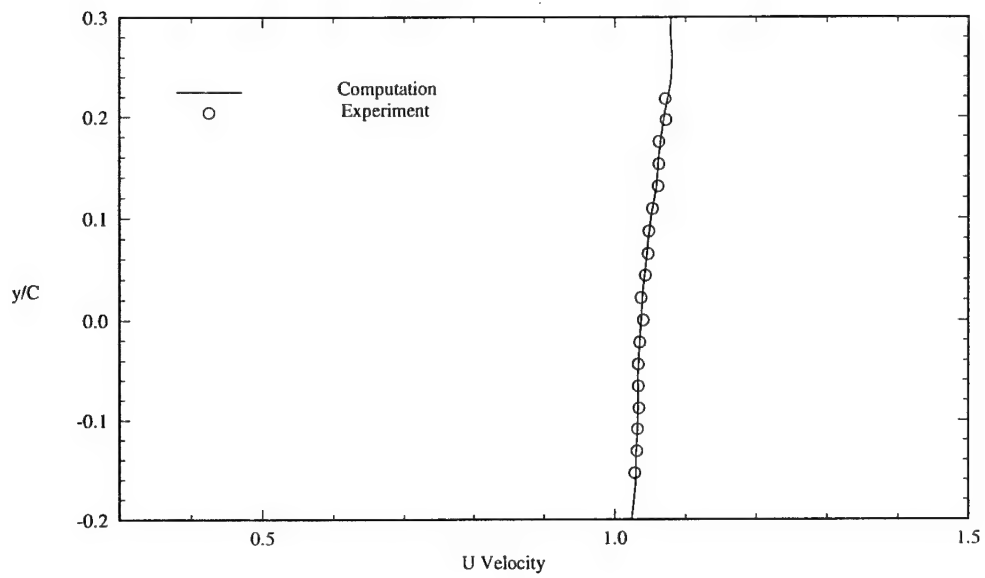


Figure 4.4: Velocity profiles at the upstream face of the test box, $\frac{x}{C} = -0.259$.

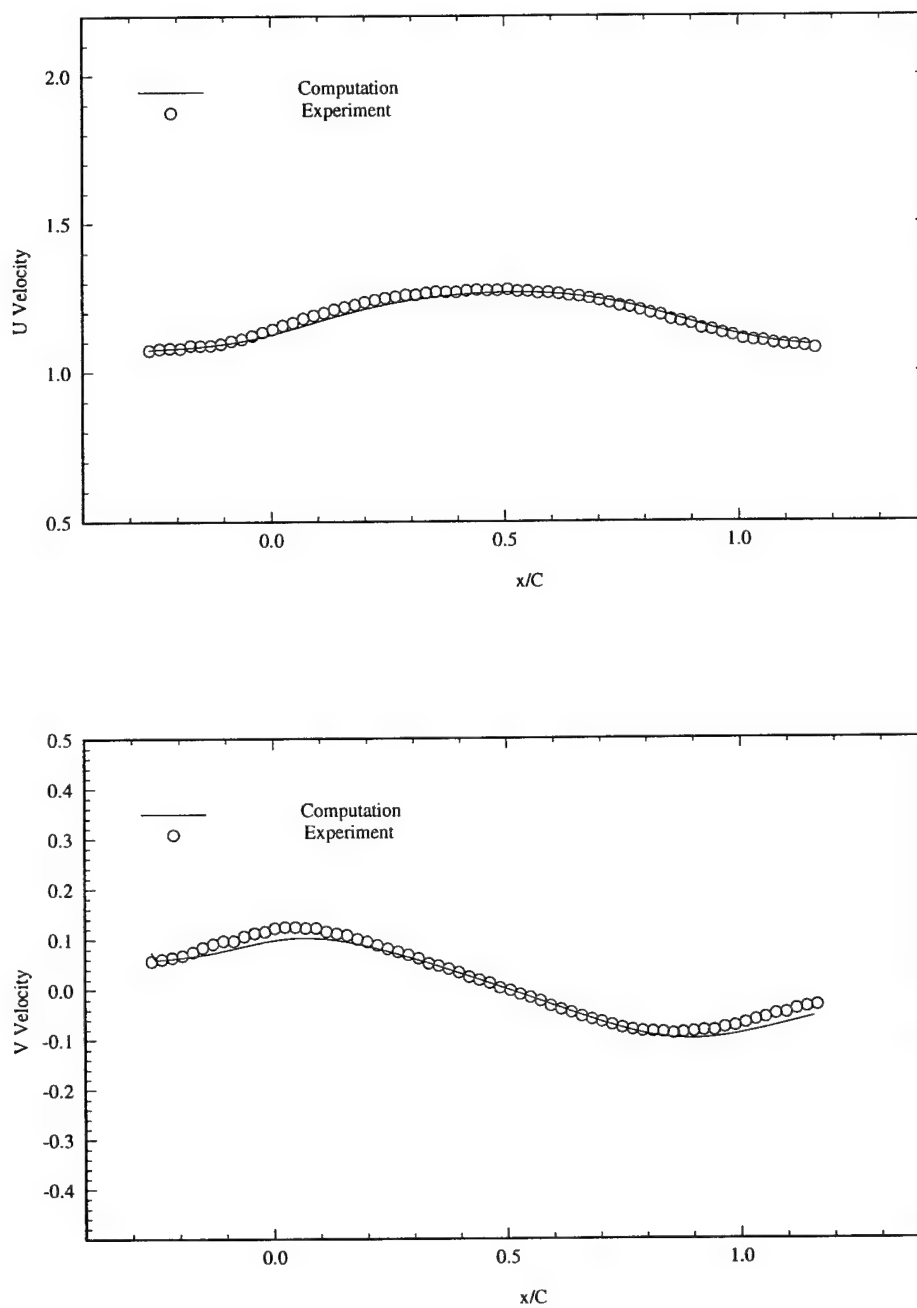


Figure 4.5: Velocity profiles at the top face of the test box, $\frac{y}{C} = 0.219$.

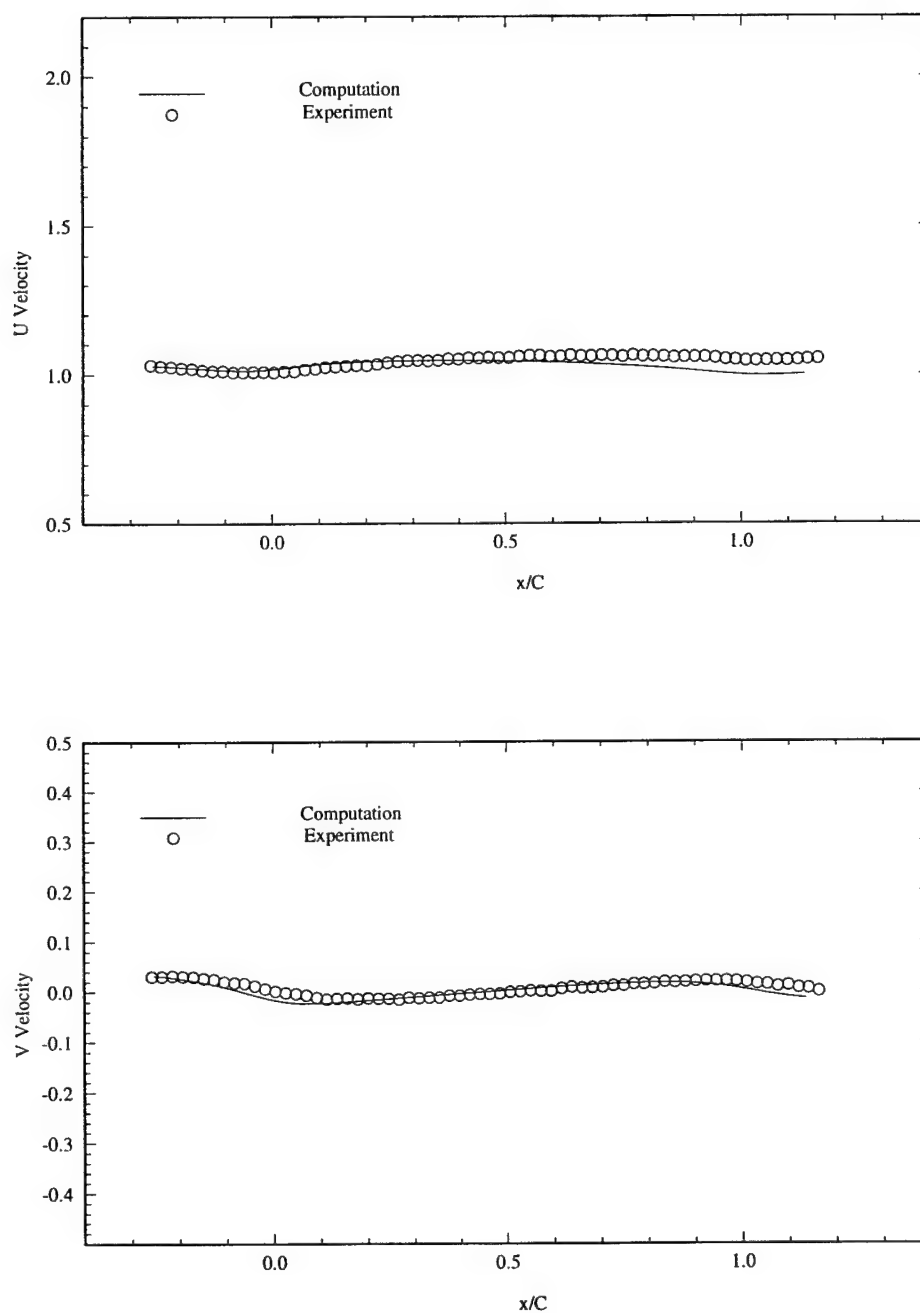


Figure 4.6: Velocity profiles at the bottom face of the test box, $\frac{y}{C} = -0.153$.

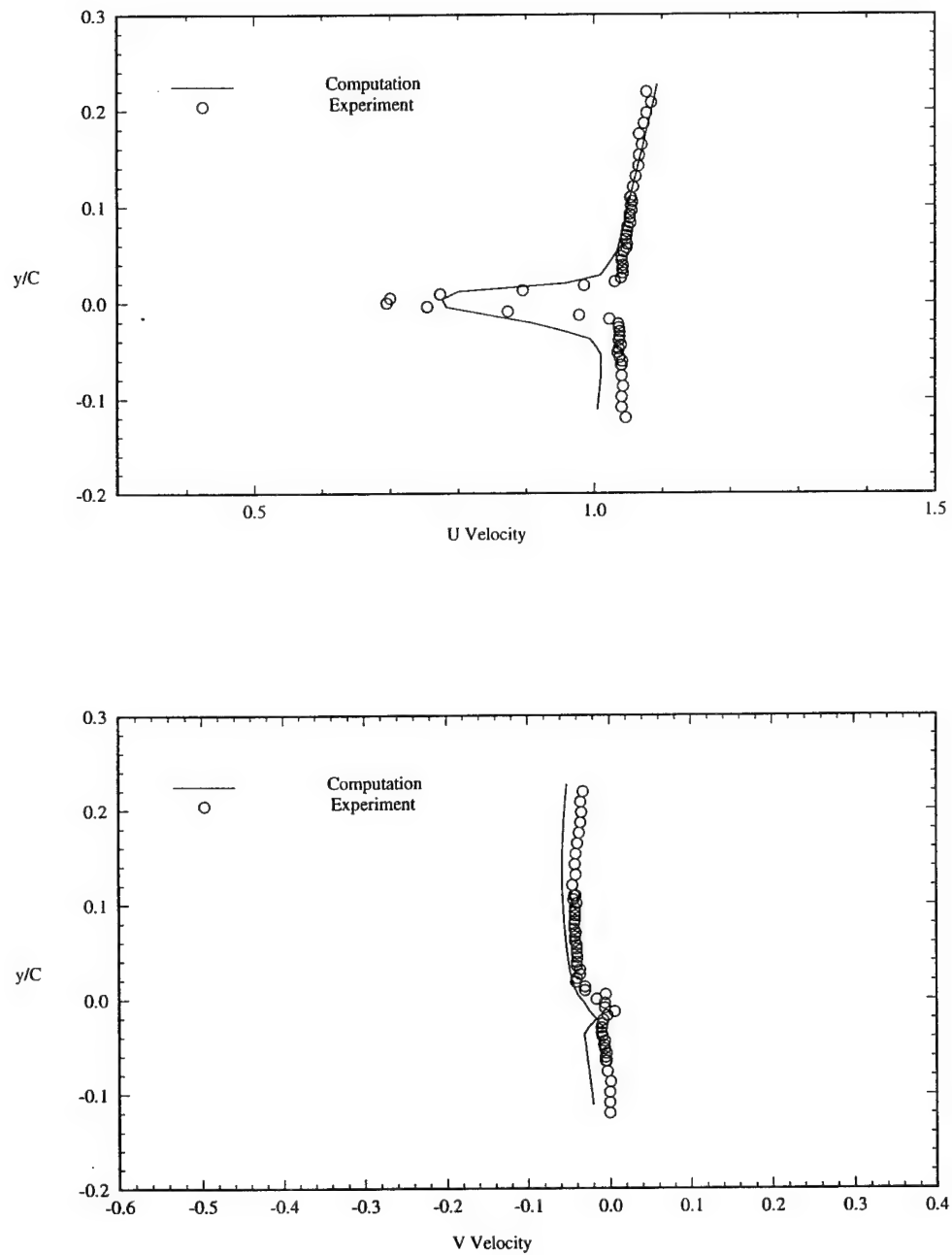


Figure 4.7: Velocity profiles at the downstream face of the test box, $\frac{y}{C} = 1.163$.

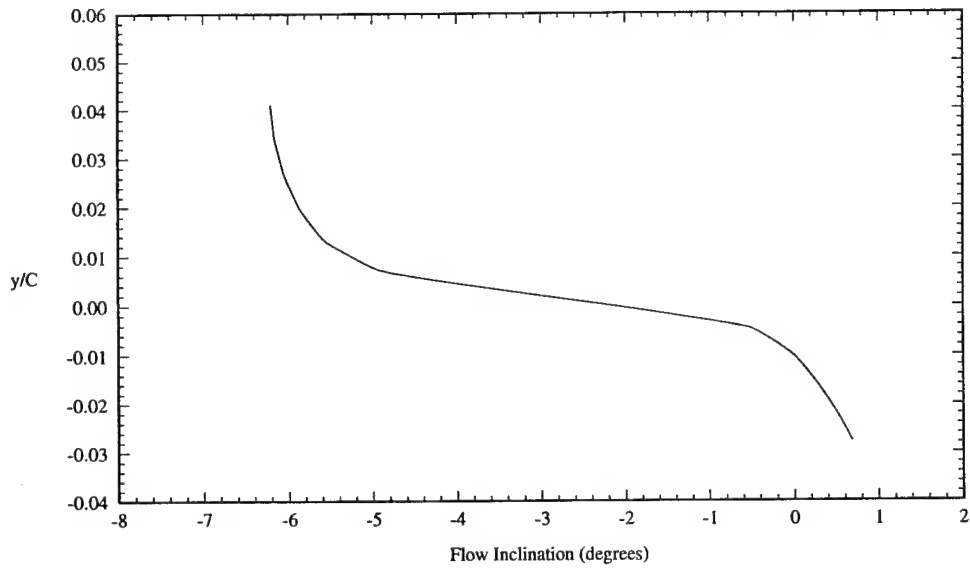
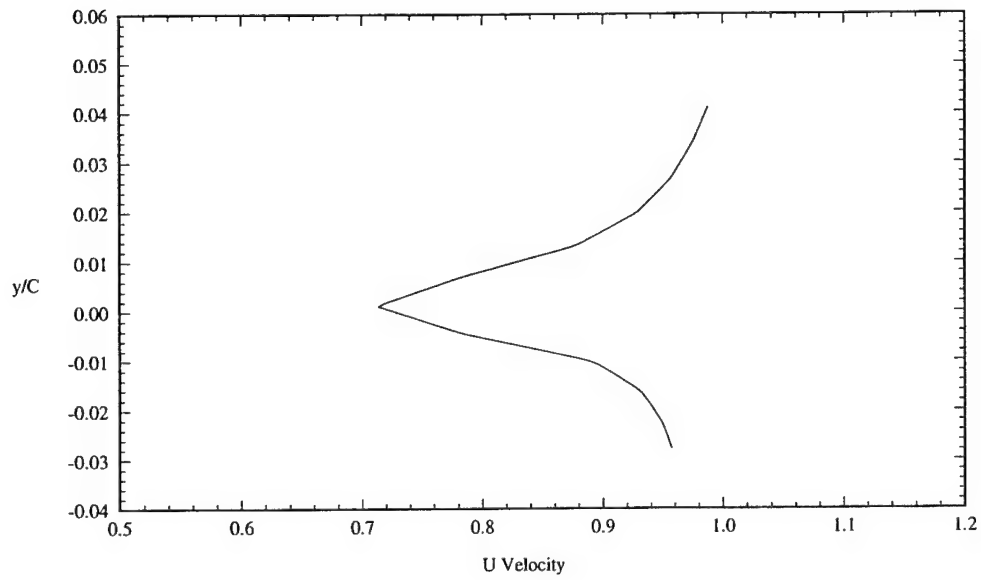


Figure 4.8: Wake profiles near the trailing edge, $\frac{x}{C} = 1.05$.

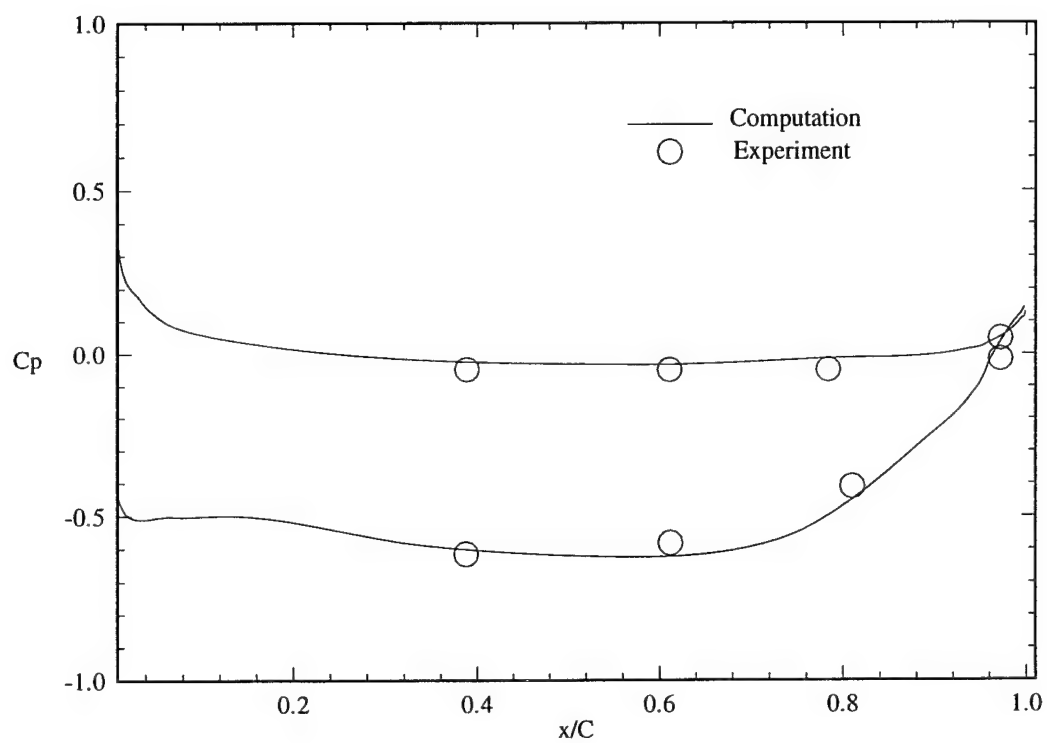


Figure 4.9: Steady flow surface pressure coefficients.

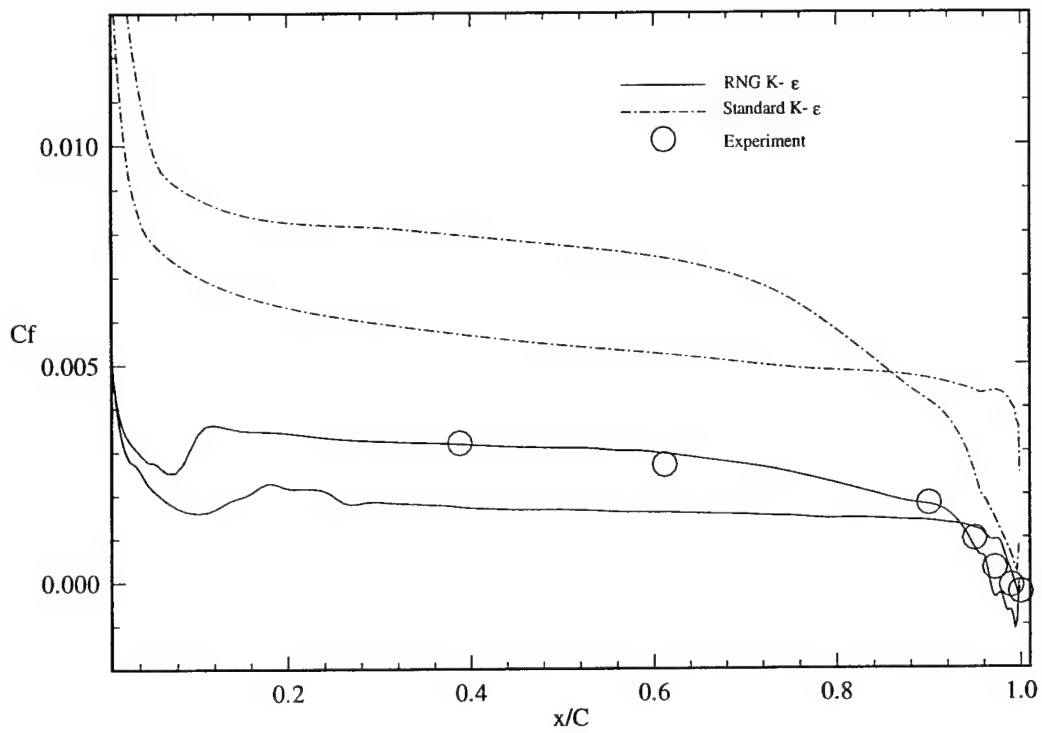


Figure 4.10: Steady flow skin friction coefficients.

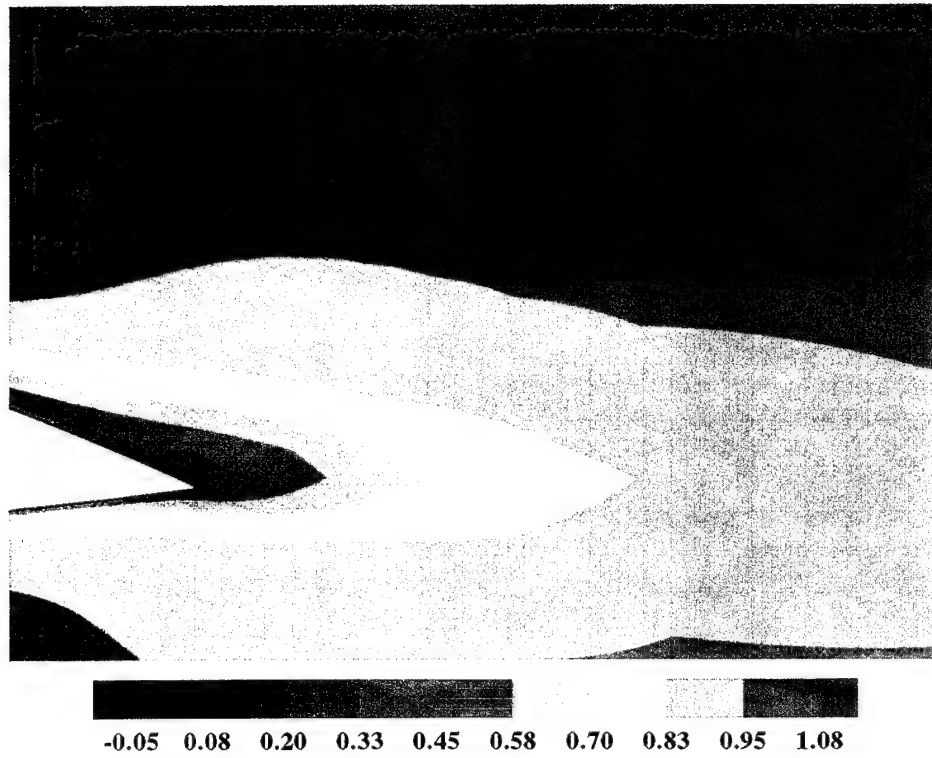
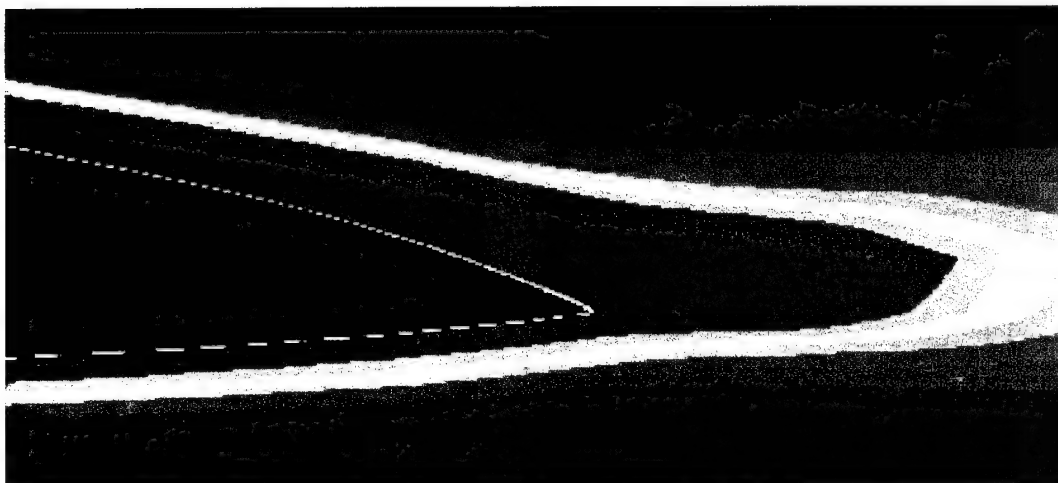
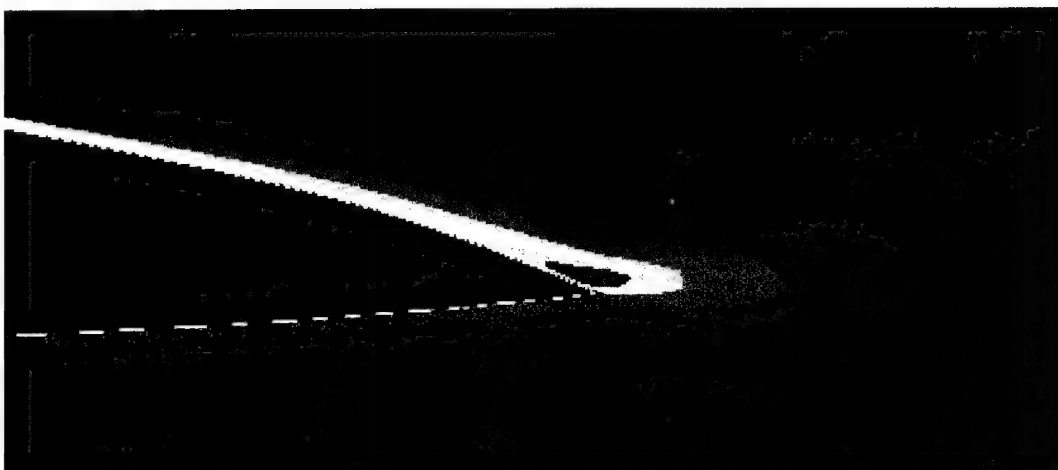


Figure 4.11: Streamwise velocity contours at the trailing edge of the foil, Separation region on the suction side is clearly visible.



Standard $K-\epsilon$ Model



RNG $K-\epsilon$ Model

Figure 4.12: Turbulence kinetic energy contours at the trailing edge of the foil. Red color for standard $K - \epsilon$ model indicates a level of $\simeq 2\% - 5\%$ when normalized by free stream kinetic energy, while red color for RNG $K - \epsilon$ model represents $\simeq 2\%$. Blue color shows $\simeq 10^{-3}\%$ for both models.

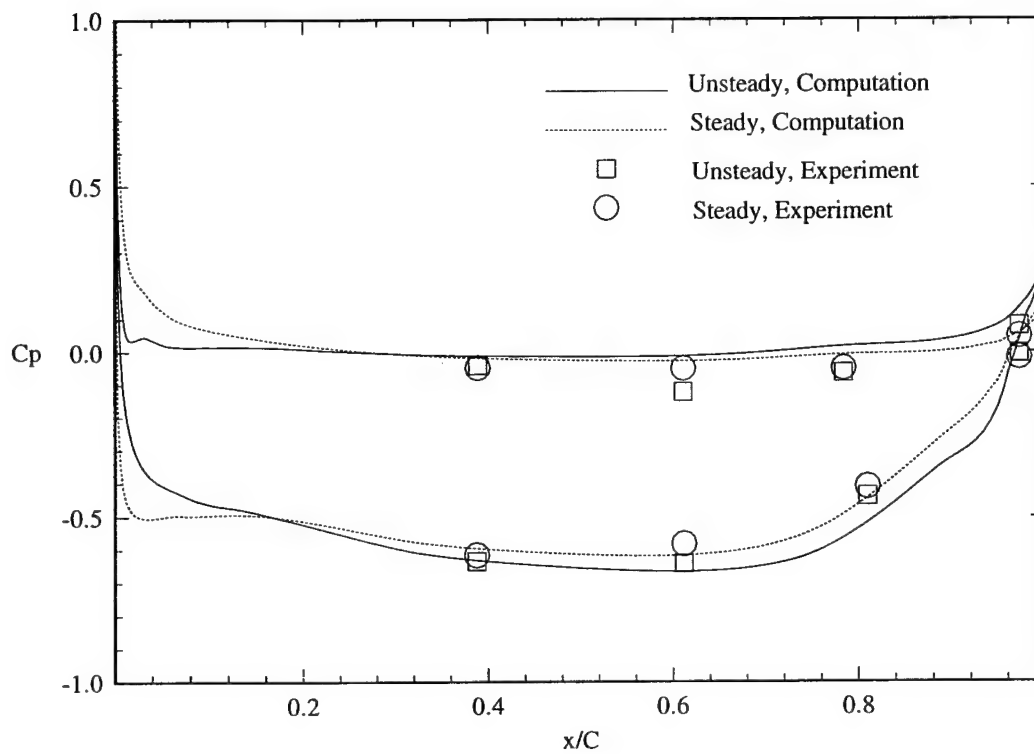


Figure 4.13: Zeroth Harmonics of the surface pressure coefficients.

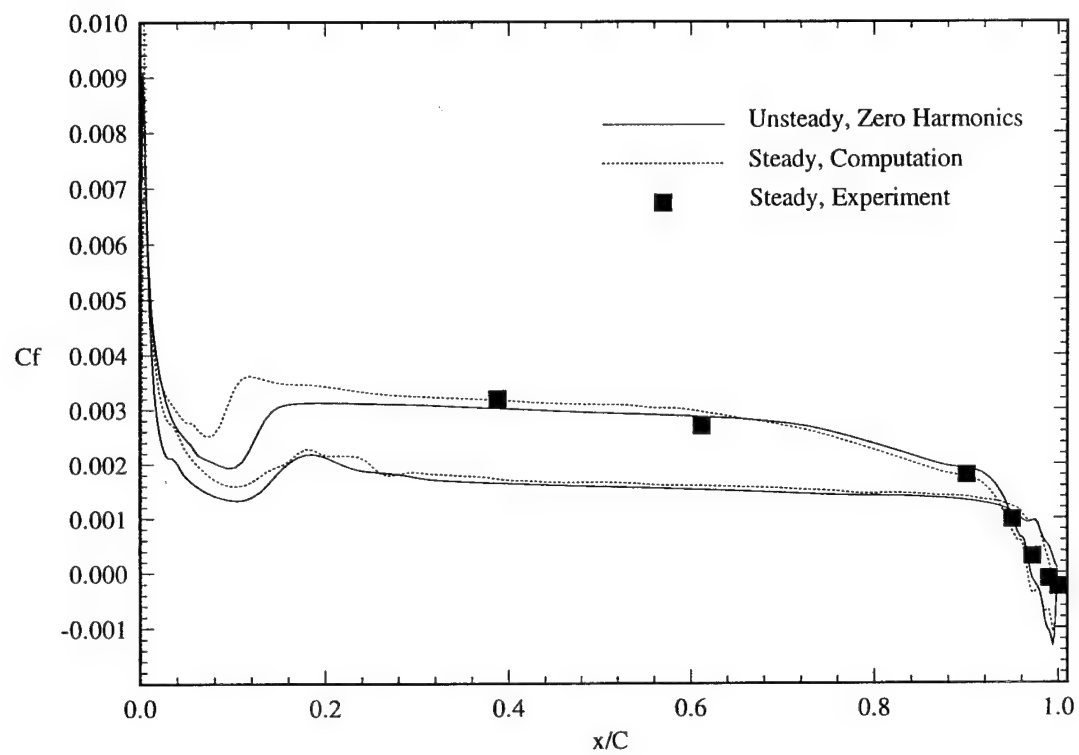


Figure 4.14: Comparison of the skin friction coefficient of steady flow and the mean C_f of unsteady flow.

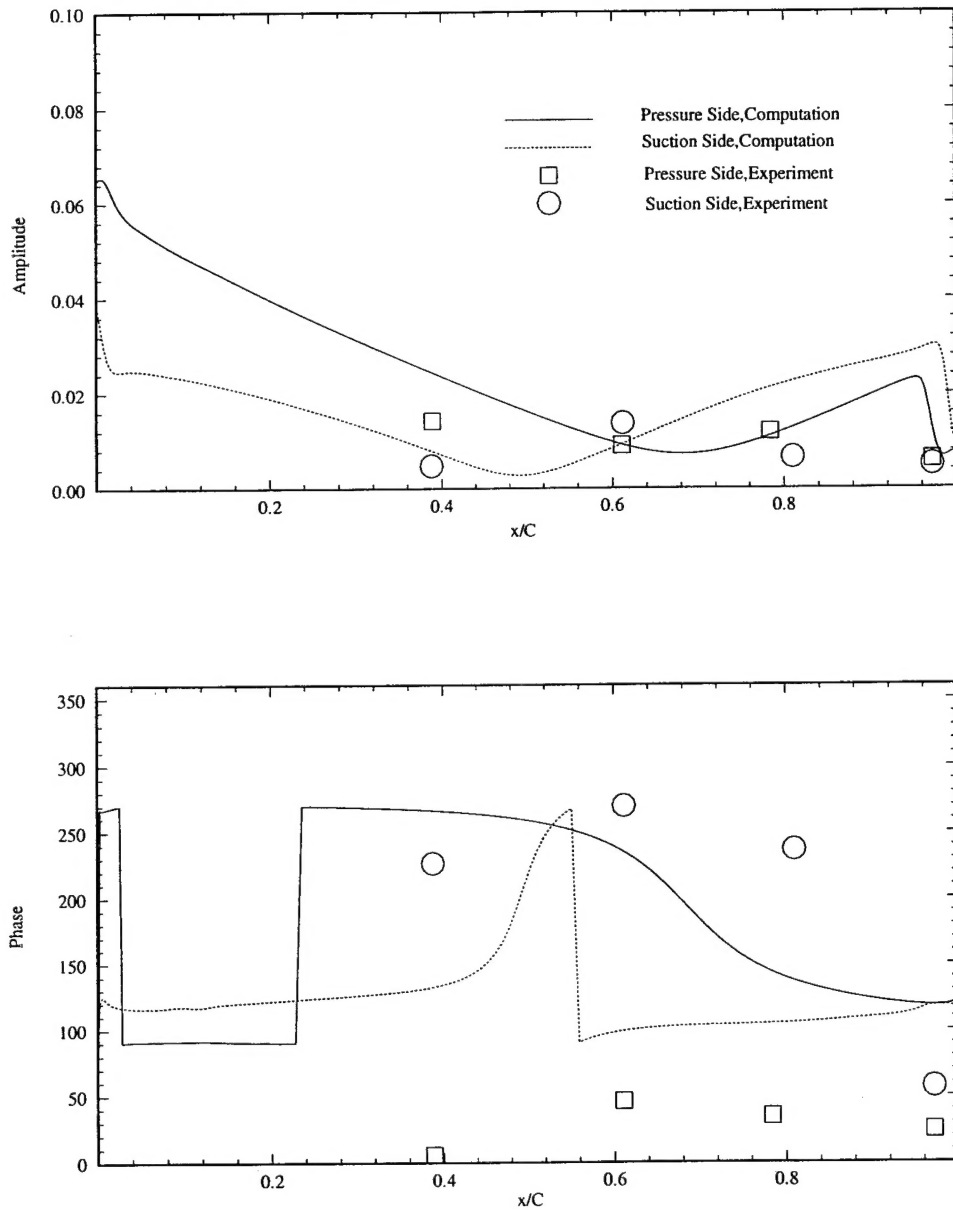


Figure 4.15: First Harmonics of the surface pressure coefficients.

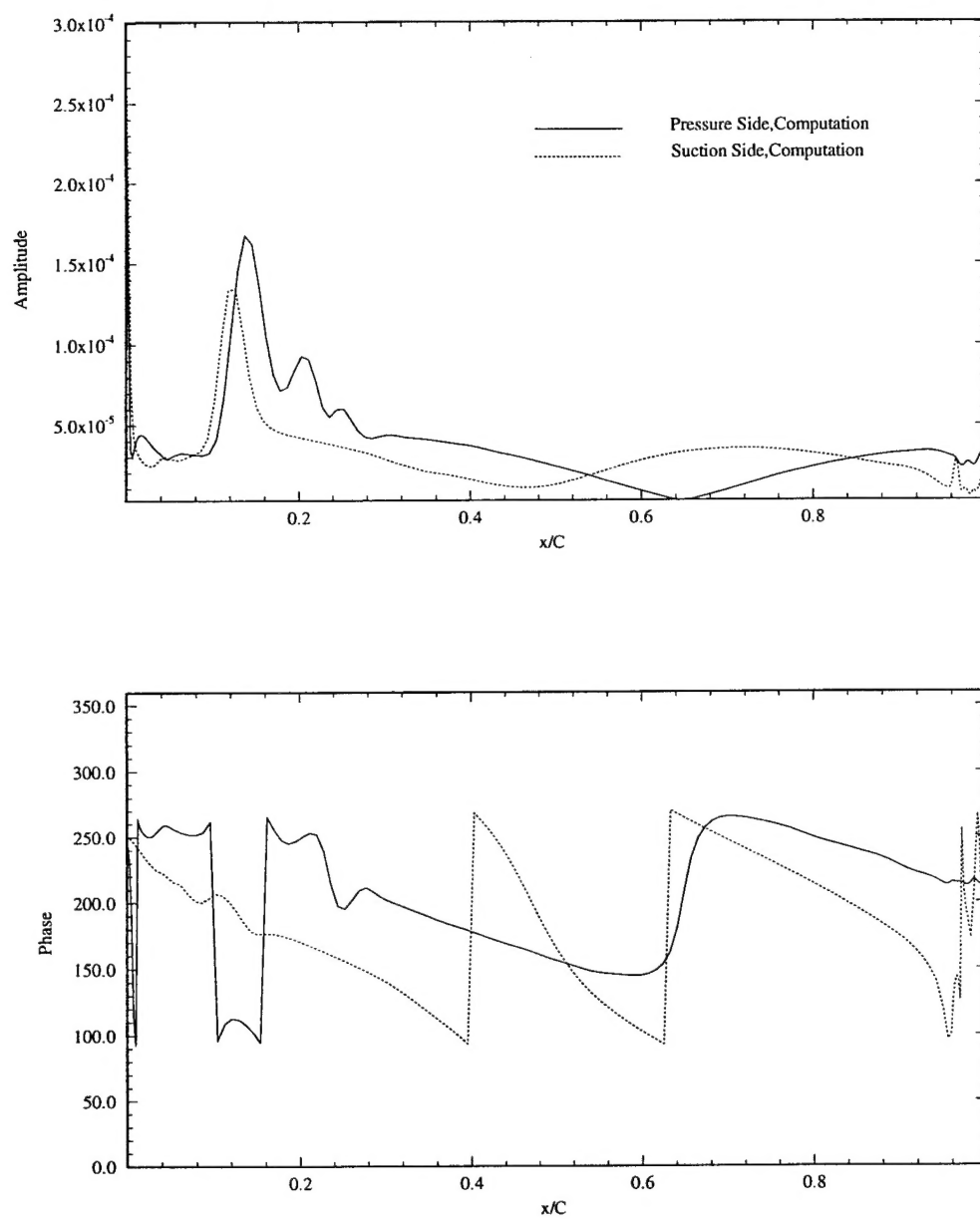


Figure 4.16: First Harmonics of the skin friction coefficients.

List of Figures

- 2.1 Mean-velocity profile, $z_+ = 0$ corresponds to the rigid wall; the dashed line is the law of the wall $u_+ = 5.5 + 2.5 \ln z_+$; $U_{max}/u_* = 18.6$, $U_{max}/U_m = 1.148$ 20
- 2.2 Root-mean-square velocity fluctuations normalized by the wall shear velocity: \times , v_x^{rms} ; \square , v_y^{rms} ; \triangle , v_z^{rms} . (a) in global coordinates; (b) in wall coordinates. 21
- 2.3 Reynolds stress $-\langle v_x v_z \rangle$: (a) in global coordinates; (b) in wall coordinates. Correlation coefficient $-\langle v_x v_z \rangle / v_x^{rms} v_z^{rms}$: (c) in global coordinates. 22
- 2.4 Root-mean-square vorticity fluctuations normalized by the mean shear: \times , $\omega_x \nu / u_*^2$; \square , $\omega_y \nu / u_*^2$; \triangle , $\omega_z \nu / u_*^2$ in wall coordinates. 23
- 2.5 Distribution of eddy viscosity $\frac{\nu_{eddy}}{\nu H_+}$ in open channel flow. Crosses - measurements. Dashed line - (18) Solid line - (19) model. 24
- 2.6 (a) Root mean-square pressure fluctuations normalized by the wall shear velocity p_{rms}/u_*^2 ; (b) Ratio of root mean-square pressure fluctuations to the mean kinetic energy. 25
- 2.7 Near-free-surface behavior of flow characteristics. The limiting operator $\hat{\mathcal{F}}$ is applied to: \times , \mathcal{E} ; \triangle , $\langle d(v_x v_z)/dz \rangle$; \square , $\langle dv_x/dz \rangle$; \circ , $\omega_{x,y}^{rms}$. The ratios of $K(z_{fs})/K(0)$ and $\omega_z^{rms}(z_{fs})/\omega_z^{rms}(0)$ are shown by $*$ and \bullet , respectively. Solid line is $e^{-z_{fs}/\lambda}$ with $\lambda \approx 0.08H$. z_{fs} is the distance from the free surface. 26
- 2.8 Two-dimensional spectrum of characteristic surface frequencies. Lines of constant $\log(\Omega_h(k))$ as the function of k_x/k_d , k_y/k_d are shown. 27

2.9	Spectra of characteristic surface frequencies $\Omega_h(k)$ as the function of k/k_d for $F_i \approx 0.55$ (solid line). The dashed line is $\Omega(k) = (gk)^{1/2}$	28
2.10	One dimensional spectra of surface height correlator $U_h(k)/h_{rms}^2$ (solid line); the normal velocity at the surface correlator $U_{v_z}(k)/\langle v_z^2 \rangle _{fs}$ (dashed line); the tangential velocity at the surface correlator $10^{-1}U_{v_{x,y}}(k)/\langle v_{x,y}^2 \rangle _{fs}$ (dot-dashed line) as the function of k/k_d . Dot line is $1/k^{5/3}$	29
4.1	Steady flow static pressure contours around the foil.	43
4.2	Steady flow streamwise velocity contours.	44
4.3	Steady flow vertical velocity contours.	45
4.4	Velocity profiles at the upstream face of the test box, $\frac{x}{C} = -0.259$	46
4.5	Velocity profiles at the top face of the test box, $\frac{y}{C} = 0.219$	47
4.6	Velocity profiles at the bottom face of the test box, $\frac{y}{C} = -0.153$	48
4.7	Velocity profiles at the downstream face of the test box, $\frac{y}{C} = 1.163$	49
4.8	Wake profiles near the trailing edge, $\frac{x}{C} = 1.05$	50
4.9	Steady flow surface pressure coefficients.	51
4.10	Steady flow skin friction coefficients.	52
4.11	Streamwise velocity contours at the trailing edge of the foil, Separation region on the suction side is clearly visible.	53
4.12	Turbulence kinetic energy contours at the trailing edge of the foil. Red color for standard $K - \epsilon$ model indicates a level of $\simeq 2\% - 5\%$ when normalized by free stream kinetic energy, while red color for RNG $K - \epsilon$ model represents $\simeq 2\%$. Blue color shows $\simeq 10^{-3}\%$ for both models.	54
4.13	Zeroth Harmonics of the surface pressure coefficients.	55
4.14	Comparison of the skin friction coefficient of steady flow and the mean C_f of unsteady flow.	56
4.15	First Harmonics of the surface pressure coefficients.	57
4.16	First Harmonics of the skin friction coefficients.	58